The DOI for this manuscript is

DOI:10.2151/jmsj.2022-046

J-STAGE Advance published date: August 3rd, 2022

Statistical Analysis of Remote Precipitation in Japan Caused by Typhoons in September

Shinichi KODAMA[1]

Atmosphere and Ocean Research Institute
The University of Tokyo, Kashiwa, Japan

and

Masaki SATOH

Atmosphere and Ocean Research Institute
The University of Tokyo, Kashiwa, Japan

July 17, 2022

----

1) Corresponding author: Shinichi Kodama, Atmosphere and Ocean Research Institute
The University of Tokyo, 5-1-5, Kashiwanoha, Kashiwa-shi, Chiba 277-8564 Japan.
Email: kodama@aori.u-tokyo.ac.jp

Abstract

During the autumn rainy season, typhoons located far from Japan sometimes cause significant precipitation in Japan. In this study, we characterized remote precipitation events in September for 40 years from 1980 to 2019. We also analyzed cases in which remote precipitation did not occur despite approaching typhoons, as well as cases in which heavy precipitation was not affected by typhoons. We characterized the environmental fields of the remote precipitation cases by comparing them with these other two types of cases.

Statistical analysis showed that remote precipitation tended to occur when the typhoons were located over the southern or southwestern oceans of mainland Japan and when the tracks of the typhoons were northward or changing to the northeast. The composite analysis of the remote precipitation cases showed that the subtropical high was retreating to the east for the two days before the remote precipitation. By contrast, the cases in which remote precipitation did not occur showed the opposite pattern: the subtropical high was strengthening to the west when typhoons were approaching over the southern or southwestern oceans of the Japanese archipelago. Furthermore, the remote precipitation occurred to the equatorward jet streak entrance of the 200 hPa jet, whereas the 200 hPa jet streak was shifted to the west in the cases where remote precipitation did not occur. The vertical cross-section of the northward water vapor flux showed that the northward water vapor inflow from the middle troposphere was larger in cases of remote precipitation than in cases in which heavy precipitation was not caused by typhoons. In addition, dynamical analysis showed that the area of remote precipitation corresponded to the region of 800–600 hPa mean quasi-geostrophic forcing for ascent and 925 hPa frontogenesis.

Keywords typhoon; remote precipitation; water vapor flux; autumn rainy season

1. Introduction

During the autumn rainy (Akisame, in Japanese) season, typhoons located far from Japan can increase the supply of water vapor in Japan, resulting in significant precipitation. Wang et al. (2009) referred to this type of precipitation as remote precipitation due to the indirect effect of typhoons and distinguished it from precipitation due to the direct effect of typhoons, i.e., the effects of the eyewall and spiral rain bands. Remote precipitation is thought to be caused generally by warm and moist northward winds to the east of the typhoons, which interact with the Akisame front.

There have been several studies on remote precipitation in Japan caused by the indirect effect of typhoons during the Akisame season. Wang et al. (2009) conducted the hypothetical typhoon vortex removal experiment for Typhoon Songda in 2004, which suggested the importance of the northward water vapor transport enhanced by the typhoon. Murata (2009) argued that in addition to the supply of water vapor, the orographic effect of mountainous terrain contributed to the remote precipitation for Typhoon Meari in 2004. Ninomiya (2013) pointed out the influence of a weak westerly shortwave trough on the remote precipitation caused by Typhoon TRIX in 1965. Moreover, Kitabatake (2002) suggested that the involvement of frontogenesis and the associated vertical motion were responsible for the heavy remote precipitation caused by Typhoon Saomai in 2000. A series of studies on Typhoon Melor in 2009 suggested that moistening in the upper atmosphere due to northward ageostrophic winds contributes to enhanced precipitation by promoting convective updraft (Saito 2019; Saito and Matsunobu 2020; Saito et al. 2022).

Remote precipitation caused by typhoons is also observed in the Baiu season (early summer rainy season). Using potential vorticity analysis, Yoshida and Itoh (2012) revealed that the indirect supply of water vapor from Typhoon Maggie in 1999 caused remote precipitation. Hirata and Kawamura (2014) statistically analyzed the remote impact on Japan of two primary tracks of typhoons in the Baiu season. In addition, Kawamura and Ogasawara (2006) and Yamada and Kawamura (2007) studied the interaction between typhoons and the Pacific-Japan pattern from the Baiu season to the Akisame season and found that the remote precipitation is related to the strengthening of the subtropical high to the east of Japan.

Research on remote precipitation and water vapor transport in East Asian regions other than Japan has also been conducted. Byun and Lee (2012) performed a statistical analysis of remote precipitation cases on the Korean Peninsula, distinguishing between typhoons that made landfall in China and those that did not. Yuan et al. (2018) conducted a statistical analysis of the remote precipitation caused by tropical cyclones in the Bay of Bengal. Yoshikane and Kimura (2005) studied the differences in the features of water vapor transport between June and September around East Asia, which suggested that a large amount of water vapor is transported in September in association with the movement of typhoons.

By contrast, a region of precipitation caused indirectly by the effects of tropical cyclones over North America is called a predecessor rain event (PRE) (Cote 2007). PRE is generally explained as a phenomenon in which tropical cyclones in the Atlantic Ocean recurve (changing track to the northeast) and move northward into the mid-latitudes, forming a rain band that stagnates over North America about 1000 km north of the tropical cyclones, resulting in heavy precipitation (Kitabatake 2012). Galarneau et al. (2010) conducted a statistical analysis of PRE over 14 years and analyzed in more detail the case of tropical cyclone Erin in 2007. Schumacher et al. (2011) studied the same tropical cyclone by conducting a sensitivity experiment with water vapor associated with TC Erin removed. They showed that although the precipitation was enhanced by water vapor from Erin, it was the environmental field that generated the precipitation, even in the absence of Erin. Moreover, Schumacher and Galarneau (2012) analyzed ensemble forecasts for the 2007 Erin and the 2008 Ike and found that the increased water vapor transport due to recurving did not necessarily enhance the precipitation. Many other studies have aimed to clarify the mechanism of PRE and the indirect effects of tropical cyclones (Bosart and Carr 1978; Ross and Kurihara 1995; Bosart et al. 2012; Moore et al. 2013).

The environmental conditions of PRE in North America and of remote precipitation in Japan are very different, and their underlying mechanisms are not necessarily the same. PRE in North America occurs over land, while remote precipitation in Japan occurs mainly over the ocean or adjacent areas. Although there are many studies of PRE, there are few statistical studies of remote precipitation cases in Japan. The purpose of this study is to identify the differences between the environmental fields of remote precipitation cases and those of cases in which remote precipitation did not occur even when typhoons were approaching. In addition, we compare remote precipitation cases with heavy precipitation cases that are not influenced by typhoons and investigate the effect of typhoons on remote precipitation from the viewpoint of water vapor flux.

The structure of this paper is as follows. Section 2 presents the data used and how the remote precipitation cases were extracted. Section 3 presents statistical data on typhoons and the results of the composite analysis. Section 4 discusses the subtropical high, water vapor flux, and dynamical lifting mechanism. Finally, Section 5 provides an overall summary.

2. Data and methods

2.1 Data

In this study, we used Best Track Data from the Regional Specialized Meteorological Center (RSMC) Tokyo-Typhoon Center, which provides information on typhoons occurring from 1951 to the present. For precipitation and other physical parameters, we used the European Centre for Medium-Range Weather Forecasts (ECMWF) Reanalysis v5 (ERA5) data, which provides a variety of physical parameters from 1950 to the present with a horizontal resolution of 0.25 degrees in latitude and longitude and 37 pressure levels from 1000 hPa to 1 hPa. Hourly data on pressure levels (Hersbach et al. 2018a), hourly data on single levels (Hersbach et al. 2018b), and monthly averaged data on single levels (Hersbach et al. 2019) were used in this study. The Global Satellite Mapping of Precipitation (GSMaP)

(Kubota et al. 2007) was used to confirm the reproducibility of the ERA5 precipitation data. The GSMaP provides hourly data for rainfall intensity from 2000 to the present in the region 60°S–60°N with a horizontal resolution of 0.1 degrees in latitude and longitude. We made a comparison between the ERA5 and the GSMaP for one typical case of remote precipitation, that is Typhoon Songda in 2004 as analyzed by Wang et al. (2009), and for monthly precipitation in September over 20 years (Supplement 1). Although there are some differences in the distribution of daily precipitation and the amount of monthly precipitation, we determined that the use of ERA5 precipitation data is reasonable.

2.2 Methods

The analysis period of this study is every September from 1980 to 2019. September was selected as the month in which remote precipitation is most likely to occur because of two factors: the occurrence of many typhoons and the Akisame front is stagnant near Japan. We first extracted the days when daily precipitation of 40 mm or more was recorded at 33 or more grid points in the rectangular domain covering a major part of Japan [130–150°E, 30–40°N], regardless of whether or not typhoons were approaching. The daily precipitation was obtained by totaling the hourly precipitation from 00 UTC to 23 UTC from the ERA5 data. The threshold value of 40 mm was selected to ensure that representative cases of remote precipitation – such as Typhoon Saomai in 2000 (Kitabatake 2002), Typhoon Meari in 2004 (Murata 2009), and Typhoon Songda in 2004 (Wang et al. 2009) – were included. Moreover, we did not set a high threshold as we did not want to reduce the number of cases too far. The grid point threshold of 33 was chosen because this represents about 1% of all grid points in the rectangular domain and excludes rainfall events that are too localized. The rectangular domain was chosen because it includes the area with monthly mean September precipitation of about 250 mm or more, calculated from the 40 years of ERA5 data covering our study period. As a result, we obtained 618 precipitation days. Up to this point, we had not considered whether or not the precipitation was due to the indirect effects of typhoons. In this study, the precipitation threshold was set at 40 mm, but 680 days were extracted with threshold of 35 mm and 531 days with threshold of 45 mm.

To define the days when typhoons were remotely located, we referred to Tsuguti and Kato (2014); we extracted the cases in which the distance between a typhoon center and a precipitation center was between 500 km and 1500 km. Typhoons in this study are those with a maximum wind speed of at least 34 knots. Typhoons above 34 knots are classified as grades 3, 4, and 5 in the Best Track Data. The typhoon center was defined as the location at 12 UTC on the day of precipitation, and the precipitation center was defined as the location of maximum daily precipitation in the rectangular domain. In the case of multiple typhoons within 500–1500 km of the precipitation center on the same day, only the typhoon closest to the precipitation center was considered. In addition, to confirm the remote impact of typhoons on precipitation areas, we referred to Galarneau et al. (2010) to check the connection between the typhoon and the precipitation; we defined the precipitation as remote if both the typhoon center and the precipitation center were surrounded by a contour with daily average precipitable water (ERA5 total column water vapor data) of 50 mm or more. For cases of remote precipitation caused by the same typhoon, we counted only the first day on which the above criteria were satisfied. As a result, we extracted 58 remote precipitation cases. Hereafter, we refer to these cases of remote precipitation in Japan as "PRE" cases, to acknowledge their similarity to PRE in North America.

We also extracted the cases in which PRE did not occur, i.e., heavy precipitation did not occur even though typhoons were approaching Japan. These cases are hereafter referred to as "non-PRE" cases. To obtain these cases, we first extracted the days when daily precipitation of less than 40 mm was recorded at all grid points in the rectangular domain. From this list, we selected the cases in which the distance between the typhoon center and the median point of the precipitation centers, which was defined from the precipitation centers of the 58 PRE cases, was between 500 km and 1500 km. Since precipitation in the non-PRE cases are small and it is not possible to define precipitation center in individual cases, the median point of the precipitation centers obtained from the 58 PRE cases was used as a provisional precipitation center. In addition, we excluded cases where the typhoons were determined to be typhoons of the extracted PRE cases. As with the PRE cases, for the non-PRE cases caused by the same typhoon, we counted only the first day on which the above criteria were satisfied. As a result, 31 non-PRE cases were extracted.

Finally, we also extracted cases of heavy precipitation that were not due to the influence of typhoons. We defined the days when daily precipitation of 80 mm or more was recorded at 33 or more grid points in the rectangular domain. A precipitation threshold of 40 mm would result in a large number of cases to be extracted, so we set it at 80 mm, taking into account the number of PRE and non-PRE cases. Next, we selected the cases in which the distance between the typhoon center and the precipitation center was more than 2000 km, as well as cases for which typhoons were not observed on the Best Track Data. Precipitation cases due to tropical depression (maximum wind speed of less than 34 knots, grade 2 on the Best Track Data) or to an extratropical cyclone that transformed from a typhoon (grade 6 on the Best Track Data) were also excluded. For cases of heavy precipitation on consecutive days, we counted only the first day. As a result, 24 cases of heavy precipitation without the influence of typhoons were extracted. These cases are hereafter referred to as "non-typhoon" cases.

3. Results

3.1 Statistical data

Figure 1 shows the locations of typhoon centers and precipitation centers for the PRE, the non-PRE, and the non-typhoon cases, as well as the rectangular domain used to define the precipitation location. Statistical analysis of the PRE cases showed that the typhoon centers at the time of PRE occurrence were widely distributed in the zonal areas over the southern and southwestern oceans of Japan between 120°E and 150°E (Fig. 1a). The precipitation centers were also widely distributed within the rectangular domain [130–150°E, 30–40°N] and were located over oceans where the orographic effect is not effective (Fig. 1b). Most of the tracks of the typhoons were northward or recurving, with few westward typhoon tracks (Figs. 2a–2d). The distances between the typhoon center and the precipitation center were between 500 km and 1500 km, but distances of more than 1000 km were more frequent (Fig. 3a). Examination of the direction of the precipitation centers from the typhoon centers indicated that PRE tended to occur to the north to northeast of the typhoons (Fig. 3b). In other words, PRE tended to occur when the typhoons were located over the southern or southwestern oceans of the Japanese archipelago. Four cases were excluded from Fig. 3b because their azimuths were not within 90 degrees. Examination of the central pressure of the typhoons at the time of PRE occurrence showed that typhoons above 980 hPa, which were relatively weak, still caused PRE (Fig. 3c). For the typhoons that persisted for more than 6 days, we compared the time of minimum central pressure with the time of central pressure at PRE occurrence. We found that six typhoons caused PRE before the time of minimum central pressure, five typhoons caused PRE at the time of minimum central pressure, and 18 typhoons caused PRE after the time of minimum central pressure. This result is similar to that of the statistical analysis of North American PRE (Galarneau et al. 2010), in which tropical cyclones tended to weaken when PRE occurred. Finally, Figure 4 shows the relationship between the central pressure of the typhoons and the maximum daily precipitation. One case with extremely high precipitation was excluded.

Figure 4 indicates that the intensity of the remote precipitation is not affected by the intensity of typhoons. Based on this result, we did not take into consideration the effects of the difference in the strength of typhoons on precipitation in the following analysis. The mean of the maximum daily precipitation of the 58 PRE cases was about 125 mm.

For the non-PRE cases, the typhoon centers were widely distributed, similar to those of the PRE cases (Fig. 1c vs 1a), but the typhoons tended to be located more eastward than those of the PRE cases. Most of the tracks of the typhoons were northward or recurving, but some typhoons moved westward without recurving (Figs. 2e–2h). By comparing Fig.3c and 3d, it is evident that whether PRE occurred or not was independent of the strength of the typhoons. This shows once again that we do not have to take into consideration differences in the strength of typhoons.

The distribution of the precipitation centers of the 24 non-typhoon cases is shown in Fig. 1d. It is not so different from that of the PRE cases (Fig. 1b). The mean daily maximum precipitation of the extracted cases was about 157 mm.

3.2 Composite analysis

1) PRE cases

Time evolution of the 500 hPa geopotential height (contour), the precipitable water (shaded), and the vertical integrals of water vapor flux (vector) were investigated by composite analysis (Fig. 5). These are the composite maps during the period from Day–2 (two days before PRE occurrence) to Day+1 (one day after PRE occurrence). The time of PRE occurrence was defined as 12 UTC on the day of occurrence, which is the same as the definition of the locations of typhoon centers. For this reason, we used 12 UTC data for each case. In these composite analyses, we referred to Galarneau et al. (2010); the precipitation centers of the 58 PRE cases were shifted to their median point on Day0. The composite maps for Day–2, Day–1, and Day+1 were obtained after shifting the latitude and longitude by the same amount as on Day0 in each case. The results show that the high precipitable water exceeding 50 mm entered the rectangular domain by Day0, and the subtropical high (represented by the 5880 m line) was retreating to the east from Day–2 to Day0. The movement of the western flank of the subtropical high retreating to the eastward appears to be particularly significant. The retreat of the subtropical high is similar to that seen in the cases of tropical cyclones over the East China Sea (Byun and Lee 2012). Moreover, the clear northward water vapor flux was observed between the typhoons and the subtropical high on Day0 and Day+1. The 200 hPa geopotential height (black contour), the 200 hPa isotach (blue contour), the 700 hPa vertical velocity (shaded), and the 850 hPa horizontal wind (vector) from Day–2 to Day+1 were investigated by composite analysis (Fig. 6). The jet streak at 200 hPa intensified by Day0 and was mostly stagnant from Day–2 to Day+1. The trough was located upstream of the jet streak, west of the precipitation area. Moreover, the precipitation area (represented by the median point of precipitation and the 700 hPa ascending basin) was located on the equatorward jet streak entrance of the 200 hPa jet on Day0. This positional relationship is consistent with the PRE statistical analyses for North America and East Asia (Galarneau et al. 2010; Byun and Lee 2012; Moore et al. 2013; Yuan et al. 2018). In the lower troposphere at 850 hPa, northward horizontal winds were also observed on Day0 and Day+1. The 850 hPa equivalent potential temperature gradient on Day0 is relatively large over Japan, indicating a baroclinic zone (Fig. 7a). Weather maps of individual cases confirmed that a front was located near Japan in many cases. To identify the layer in which water vapor entered the precipitation areas, we show the vertical cross-section of northward water vapor flux between 130°E and 150°E along the latitude 30°N, which corresponds to the lower edge of the rectangular domain (Fig. 7b). This shows that the water vapor flux entered up to the middle troposphere at 500 hPa. The details of the water vapor flux are discussed below.

2) Non-PRE cases

We constructed composite maps for the 16 non-PRE cases in which the typhoon centers were located within [130–140°E, 20–30°N] on Day0. The area was chosen because the typhoon centers were clustered there. The non-PRE cases do not define the precipitation center of each case, so the operation of shifting is not performed as in the PRE cases. Figure 8 is the same as Figure 5 but for the non-PRE cases. In contrast to the PRE cases (Fig. 5), the high precipitable water exceeding 50 mm did not enter the rectangular domain from Day–2 to Day-0. In addition, the subtropical high was strengthening to the west from Day–2 to Day0; this was in contrast to the PRE cases, where the subtropical high was retreating. Moreover, the clear northward water vapor flux was not observed from Day–2 to Day0. Figure 9 is the same as Figure 6 but for the non-PRE cases. This shows that the jet streak entrance was located more westward in the non-PRE cases than in the PRE cases. A similar result was obtained from previous East Asian PRE analysis (Yuan et al. 2018). The jet streak was weaker on Day–2 and Day–1, possibly due to the absence of an upstream trough. The 850 hPa northward horizontal winds were not observed from Day–2 to Day0. In addition, the 850 hPa equivalent potential temperature for the non-PRE cases on Day0 had a weaker gradient than in the PRE cases, indicating that the presence of the front cannot be clearly confirmed compared to the PRE cases (Fig. 10). The northward water vapor flux component was hardly seen compared to that of the PRE cases (not shown).

3) Non-typhoon cases

In the non-typhoon cases, as in the PRE cases, we made composite maps by aligning the precipitation centers of the 24 cases to their median point. On Day0, the subtropical high extended far to the west, and the precipitation area was located on the equatorward jet streak entrance of the 200 hPa jet (Figs. 11a, b). The 850 hPa equivalent potential temperature on Day0 indicates that a baroclinic zone locates over mainland Japan, as in the PRE cases (Fig. 11c). Although the northward water vapor flux component was observed in the lower troposphere at around 900 hPa, it was not clearly seen in the middle troposphere

(Fig. 11d). The northward water vapor flux was smaller than that in the PRE cases (Fig. 7b). The details of the water vapor flux in the non-typhoon cases are also discussed below.

4. Mechanisms for PRE occurrence

4.1 Extension of the subtropical high

The composite analysis of the PRE cases showed that the subtropical high was retreating to the east from Day–2 to Day0, while the non-PRE cases showed it strengthening to the west; the tendencies of the extension of the subtropical high are opposite for the PRE cases and the non-PRE cases. Because the typhoons on Day0 in the non-PRE cases were located more eastward than in the PRE cases (Fig. 1), we compared the tendencies of the extension of the subtropical high using the cases in which the typhoons are located in about the same area. Composite maps were created for 16 non-PRE cases in which the typhoon centers on Day0 were located within the area [130–140°E, 20–30°N]. Then, we analyzed 18 PRE cases in which the typhoon centers were located within the same area. The time series of the composite of 500 hPa geopotential height averaged over the region [130–140°E, 27.5–32.5°N] is shown in Fig. 12, which shows the change in the geopotential height from 48 hours before PRE occurrence. The region [130–140°E, 27.5–32.5°N] was chosen because water vapor was particularly entering the precipitation area from that region. The periodic variations for both the PRE and the non-PRE cases represent the daily variation in the subtropical high. The change in the geopotential height from Day–2 (–48 h) to Day0 shows a decreasing tendency in the PRE cases and an increasing tendency in the non-PRE cases, confirming the characteristic differences in the extension of the subtropical high between the two groups. In this analysis, the extension of the subtropical high was considered to be the 500 hPa geopotential height averaged over the region [130–140°E, 27.5–32.5°N]. Therefore, the influence of the trough located to the west identified in the PRE cases (Fig. 6c) and the ridge in front of the typhoon identified in the non-PRE cases (Fig. 9c) are considered. We only confirmed the extension change of the subtropical high, but a trough and ridge may contribute to the mechanism of the extension change of the subtropical high.

In the non-PRE cases, the area of the jet streak entrance was located more to the west than in the PRE cases, and there was no clear baroclinic zone over Japan. Mid-latitude factors such as a trough, a jet streak, and a front are important in determining whether remote precipitation will eventually occur. However, the extension of the subtropical high, which influences the amount of northward water vapor transport, may also be important in determining whether or not PRE occurs when typhoons are approaching. The dynamical interaction between typhoons and the subtropical high has been discussed in previous studies on remote precipitation during the Baiu season. Kawamura and Ogasawara (2006) and Yamada and Kawamura (2007) revealed that typhoons excite the PJ pattern through convective heating, locally strengthening the western ridge of the subtropical high. Yoshida and Itoh (2012) suggested that typhoons advect low potential vorticity from low latitudes and the subtropical high strengthens to the west. Moreover, Hirata and Kawamura (2014) showed that typhoons produce negative absolute vorticity to the east and affect the subtropical high. Our results show that when typhoons are approaching, the subtropical high can both retreat and strengthen, so more detailed studies about the relationship between typhoon, subtropical high, and trough are needed.

4.2 Northward water vapor flux

Vertical cross-sections of the northward water vapor flux component for the PRE cases and the non-typhoon cases showed that water vapor flux was observed mainly in the lower troposphere in both cases, but differed between the two cases in the middle troposphere (Figs. 7b vs 11d). To better clarify the difference between the precipitation mechanism in the PRE cases and the non-typhoon cases, we analyzed this difference in the water vapor flux further. The water vapor flux is a product of air density ρ, water vapor mixing ratio q_v, and wind speed v. We investigated whether q_v or v contributed more to the difference in the water vapor flux by ignoring the contribution of ρ, because its difference is smaller than that of q_v or v. In the following analysis, we also focused only on the northward component as water vapor flux toward Japan. The difference in the water vapor flux between the PRE cases and the non-typhoon cases can be expressed by linear decomposition as follows (1). Sekizawa et al. (2019) applied linear decomposition of the water vapor flux difference to a case of heavy rainfall in Japan.

$$\Delta(\boldsymbol{qv}) = (\boldsymbol{qv})_{\boldsymbol{PRE}} - (\boldsymbol{qv})_{\boldsymbol{NT}}$$

$$= \boldsymbol{q}_{PRE} \cdot \boldsymbol{v}_{PRE} + (\boldsymbol{q}'\boldsymbol{v}')_{PRE} - \boldsymbol{q}_{NT} \cdot \boldsymbol{v}_{NT} - (\boldsymbol{q}'\boldsymbol{v}')_{NT}$$

$$= (\boldsymbol{q}_{NT} + \Delta\boldsymbol{q})(\boldsymbol{v}_{NT} + \Delta\boldsymbol{v}) + (\boldsymbol{q}'\boldsymbol{v}')_{PRE} - \boldsymbol{q}_{NT} \cdot \boldsymbol{v}_{NT} - (\boldsymbol{q}'\boldsymbol{v}')_{NT}$$

$$= \boldsymbol{q}_{NT} \cdot \Delta\boldsymbol{v} + \Delta\boldsymbol{q} \cdot \boldsymbol{v}_{NT} + \Delta\boldsymbol{q} \cdot \Delta\boldsymbol{v} + (\boldsymbol{q}'\boldsymbol{v}')_{PRE} - (\boldsymbol{q}'\boldsymbol{v}')_{NT} \qquad (1)$$

Here, the values with subscripts *PRE* and *NT* represent the PRE and the non-typhoon cases, respectively, and Δ represents the difference between the two cases [$\Delta(\,) = (\,)_{PRE} - (\,)_{NT}$]. The physical quantity in bold represents the respective member mean for each case, and $(\,)'$ represents the deviation from the member mean. In addition, the $\boldsymbol{qv}$ in the first line of equation (1) is obtained by calculating the qv for each member and then averaging over the number of members. The first term $\boldsymbol{q}_{NT} \cdot \Delta\boldsymbol{v}$ in the fourth line of equation (1) represents the contribution from the anomaly in the wind speed, the second term $\Delta\boldsymbol{q} \cdot \boldsymbol{v}_{NT}$ represents the contribution from the anomaly in the water vapor mixing ratio. The value of the fourth term $(\boldsymbol{q}'\boldsymbol{v}')_{PRE}$ and the fifth term $(\boldsymbol{q}'\boldsymbol{v}')_{NT}$ is smaller than the third term $\Delta\boldsymbol{q} \cdot \Delta\boldsymbol{v}$. The results up to the third term in equation (1) are shown in Fig. 13. The contribution from the anomaly in wind speed (Fig. 13a) was the largest; that is, the contribution of the wind speed to the difference in the northward water vapor flux component was larger than that of the water vapor mixing ratio. The difference in the water vapor flux between the PRE cases and the non-typhoon cases can be approximated by the first term of equation (1) [$\Delta(\boldsymbol{qv}) \cong \boldsymbol{q}_{NT} \cdot \Delta\boldsymbol{v}$]. It is interesting that the effect of the water vapor flux is also observed above the middle troposphere in the PRE cases. It is known that deep northward water vapor inflow from the lower to the upper layers contributes to enhanced PRE precipitation (Saito and Matsunobu

2020; Saito et al. 2022). The difference in the vertical structure of the water vapor flux, and the contribution of the wind speed to the water vapor flux that cased this difference, may be related to the environmental field of both cases. In the PRE cases, the typhoons and the subtropical high were located side by side, resulting in the strong pressure gradient, and the warm and moist southerly winds between them impinged upon the front, leading to heavy precipitation. By contrast, in the non-typhoon cases, the southwesterly winds around the subtropical high impinged upon the front, leading to heavy precipitation. The detail of how these two environmental fields led to the difference in the water vapor flux in the middle troposphere is a subject for future studies.

4.3 Dynamical lifting mechanism

By comparing the PRE cases, the non-PRE cases and the non-typhoon cases, some characteristics of the PRE occurrences have been more identified, but the dynamical lifting mechanism is not yet clear. We will discuss the dynamical mechanism in correspondence with the results obtained in Section 3.2. To investigate the lifting mechanism associated with the PRE occurrence, we calculated Q vector and compared it between the three types of cases. The Q vector was calculated by the following equation (2) (Hoskins and Pedder 1980; Ogura 2000; Kitabatake 2019). The two variables geopotential (in determining the geostrophic winds u_g, v_g) and temperature T were used in the calculations by converting the resolution of the ERA5 data to 1.25 degrees. Because the Q vector involves a lot of differential calculations and to prevent localized changes, the data was used at a reduced resolution.

$$Q \equiv \frac{d_g}{dt}\left(\frac{R}{p}\nabla_p T\right) = -\frac{R}{p}\left(\frac{\partial T}{\partial x}\frac{\partial u_g}{\partial x} + \frac{\partial T}{\partial y}\frac{\partial v_g}{\partial x}\ , \frac{\partial T}{\partial x}\frac{\partial u_g}{\partial y} + \frac{\partial T}{\partial y}\frac{\partial v_g}{\partial y}\right) \qquad (2)$$

Quasi-geostrophic forcing for upward motion is suggested in the convergence region of the Q vector and forcing for downward motion in the divergence region. The 700 hPa geopotential height (black contour), the 700 hPa temperature (red contour), the 800–600 hPa mean Q vector (vector), and the 800–600 hPa mean divergence of Q vector (shaded) were investigated by composite analysis on Day0 (Fig. 14). In the PRE cases, the Q vector convergence region was located in the extraction area [130–150°E, 30–40°N] on the northeast side of typhoons (Fig. 14a). This region coincides with the location of the 700 hPa ascending motion, and there were southerly winds at 850 hPa (Fig. 6c). In addition, the Q vector pointed toward the warm side, indicating geostrophic frontogenesis. It also confirms that the trough was located west of the Q vector convergence region. In the non-PRE cases, there was almost no convergence region of the Q vector within the extraction area [130–150°E, 30–40°N] (Fig. 14b), and in the non-typhoon cases, a clear convergence region was located around the precipitation area (Fig. 14c). Although the noise in the Q vector convergence is shown near typhoons and at high latitudes, we confirmed that there is a statistically significant difference between the Q vector convergence (averaged over the area [130.75–144.5°E, 30.5–38°N]) of the PRE and the non-PRE cases at the 5% level of significance. That area was defined based on the location of relatively heavy precipitation in the PRE cases (Supplement 2a) and Welch's t-test was used for testing. There are clear differences between the three types of cases within the extraction area, especially in the PRE cases, where quasi-geostrophic forcing for ascent was observed on the northeast side of typhoons. Previous studies of statistical analysis also confirmed Q vector convergence around precipitation area for PRE cases. (Galarneau et al. 2010; Byun and Lee 2012).

In relation to the Q vector, frontogenesis was also calculated and compared among the three types of cases. Frontogenesis for the horizontal motion of confluence and shear terms was calculated by the following equation (3) (Bluestein 1993; Ogura 2000; Kitabatake 2019). The two variables geopotential (in determining the geostrophic winds u_g, v_g) and temperature (in determining the potential temperature θ) were used in the calculations by converting the resolution of the ERA5 data to 1.25 degrees.

$$
\begin{aligned}
F_g &\equiv \frac{d_g}{dt}\left|\nabla_p \theta\right| \\
&= -\frac{1}{\left|\nabla_p \theta\right|}\left\{\left(\frac{\partial \theta}{\partial x}\right)^2 \frac{\partial u_g}{\partial x} + \left(\frac{\partial \theta}{\partial y}\right)^2 \frac{\partial v_g}{\partial y}\right\} - \frac{1}{\left|\nabla_p \theta\right|}\frac{\partial \theta}{\partial x}\frac{\partial \theta}{\partial y}\left(\frac{\partial v_g}{\partial x} + \frac{\partial u_g}{\partial y}\right) \qquad (3)
\end{aligned}
$$

Figure 15 shows the composite of 925 hPa geopotential height (black contour), the 925 hPa temperature (red contour), and the 925 hPa frontogenesis (shaded) on Day0. In the PRE cases, frontogenesis occurred from the north to the northeast of typhoons, mainly in the precipitation area (Fig. 15a). Corresponding to the analysis of 850 hPa equivalent potential temperature, frontogenesis occurred along the low-level baroclinic zone on Day0 (Fig. 7a, 15a) and was further enhanced on Day+1 (not shown). In the non-PRE cases, there was almost no frontogenesis area (Fig. 15b). In the non-typhoon cases, frontogenesis occurred around the precipitation area, confirming that it occurred along the low-level baroclinic zone (Fig. 11c, 15c). Moreover, in the PRE cases, frontogenesis was analyzed from the lower to the upper troposphere, and its value was especially strong around 900 hPa and 300 hPa (Fig. 15d). Deep convection was also analyzed from the lower to the upper troposphere just above the location of the PRE occurrence. This suggests that not only the vertical secondary circulation associated with the low-level frontogenesis but also the vertical circulation associated with the upper-level frontogenesis and the jet streak may have contributed to the PRE occurrence. These characteristics about PRE are consistent with the previous statistical analyses for North America and East Asia (Galarneau et al. 2010, in especially Fig.9; Byun and Lee 2012; Moore et al. 2013; Yuan et al. 2018).

5. Conclusions

The purpose of this study is to clarify the statistical characteristics of precipitation in Japan associated with PRE, i.e., remote precipitation indirectly caused by typhoons, in September for 40 years from 1980 to 2019. In particular, we examined the locations, the tracks, and the intensity of the typhoons that cause PRE in Japan. In addition, we studied the differences in the environmental fields between three types of cases: the cases of PRE (PRE cases), the cases in which remote precipitation did not occur (non-PRE cases), and the cases in which heavy precipitation in Japan was not affected by typhoons (non-typhoon cases).

Statistical analysis of the PRE cases showed that PRE tended to occur when the typhoons were located over the southern or southwestern oceans of mainland Japan and were moving northward or recurving. The distance between the typhoons and the precipitation areas of PRE exceeded 1000 km in most cases. PRE occurred regardless of typhoon intensity; in some cases, PRE occurred when the central pressure of the typhoons was above 980 hPa. We also found that most of the PRE occurred in the weakening phase of the typhoons. No characteristic relationship was found between the central pressure of the typhoons and the maximum daily precipitation at the time of PRE occurrence.

The results of the composite analysis of the three types of cases showed the following characteristics. Conceptual models of the environmental field on the PRE and the non-PRE cases on Day0 are shown in Fig.16. First, the subtropical high south of Japan was retreating for the PRE cases during the two days before PRE occurrence, while it was strengthening for the non-PRE cases. Second, the jet streak entrance east of the 200 hPa trough was close to the precipitation area for the PRE cases; specifically, the precipitation occurred on the equatorward jet streak entrance. Furthermore, the jet streak intensified by the time of PRE occurrence. By contrast, for the non-PRE cases, the 200 hPa jet streak entrance was located to the west compared to the PRE cases, and thus heavy precipitation was not enhanced around Japan. The absence of an upstream trough, so the jet streak structure was less distinct than in the PRE cases. Third, the 850 hPa equivalent potential temperature showed that the precipitation area was characterized by the baroclinic zone for the PRE cases and the non-typhoon cases. Fourth, the vertical cross-section of the northward water vapor flux component showed that the water vapor was transported to Japan in the PRE cases and the non-typhoon cases. In both cases, water vapor transport from the lower troposphere was prominent; in the PRE cases, water vapor transport from the middle troposphere was also observed. In addition, the contribution of the wind speed to this difference in the water vapor flux was greater than that of the water vapor mixing ratio. Fifth and finally, for the PRE and the non-typhoon cases, 800–600 hPa mean quasi-geostrophic forcing for ascent and 925 hPa frontogenesis occurred near the precipitation area; in the PRE cases, frontogenesis was analyzed from the lower to the upper troposphere, and deep convection has also been analyzed from the lower to the upper troposphere. Moreover, previous studies have discussed low potential vorticity advection as a reason for the strengthening of the upper-level jet streak (Galarneau et al. 2010; Bosart et al. 2012; Moore et al. 2013; Yuan et al. 2018). Advection of low potential vorticity from low latitudes to the precipitation area was also observed in the PRE cases in this study (not shown). However, the origin of low potential vorticity air is not clear because of the possibility of typhoons, precipitation areas, and advection from low latitudes, so we did not discuss direct relevance to the mechanism of PRE occurrence in this study.

We have shown in this study that various factors are involved in PRE occurrence in Japan. Although several characteristics are consistent with previous PRE studies, there are still factors that are not yet clear. The results of this study can be regarded as one of the PRE studies in the East Asian regions and one of the PRE (remote precipitation) studies in Japan during the Akisame season. More specifically, this study may bring us closer to achieving another goal: elucidating the impact of the occurrence environment (such as continents in North America and oceans in Japan) on the mechanism of PRE. In the case of PRE in Japan, this study could lead to the discovery of differences in the mechanism of PRE between the Baiu season and the Akisame season. The mechanism of interaction between typhoons and the subtropical high and the extent to which water vapor around typhoons contributes to PRE will require further investigation. Based on the results obtained in this study, it is hoped that the mechanisms of PRE occurrence and strengthening in Japan will be clarified.

Supplements

Supplement 1. (a) Daily precipitation (shaded; mm) on 04 September 2004 using the ERA5 data. **(b)** Same as in (a) but for using the GSMaP data. **(c)** Time series of monthly precipitation in September (mm) from 2000 to 2019 (ERA5, red; GSMaP blue). The monthly precipitation is averaged over the region [130–150°E, 30–40°N].

Supplement 2. Composite of daily precipitation (shaded; mm) on **(a)** Day0 PRE cases, **(b)** Day0 non-PRE cases, and **(c)** Day0 non-typhoon cases. The black rectangle shows the extraction area [130–150°E, 30–40°N]. The red rectangle shows the Welch's t-test area [130.75–144.5°E, 30.5–38°N].

Data Availability Statements

The data generated in this study are available from the corresponding author on reasonable request. The Best Track Data (https://www.jma.go.jp/jma/jma-eng/jma-center/rsmc-hp-pub-eg/besttrack.html) was provided by RSMC Tokyo-Typhoon Center. The ERA5 data (Climate data store: https://cds.climate.copernicus.eu/cdsapp#!/search?text=ERA5&type=dataset) was provided by ECMWF. The GSMaP data (https://sharaku.eorc.jaxa.jp/GSMaP/index_j.htm) was provided by Japan Aerospace Exploration Agency (JAXA).

Acknowledgments

This work was supported by MEXT (JPMXP1020200305) under the "Program for Promoting Researches on the Supercomputer Fugaku" (Large Ensemble Atmospheric and Environmental Prediction for Disaster Prevention and Mitigation) and Grant-in-Aid for Scientific Research (C) (21K03657) and Scientific Research (B) (20H01967) from Japan Society for the Promotion of Science (JSPS). The authors thank Kazuo Saito, staff, and students of the Dynamic Marine Meteorology section, Atmosphere and Ocean Research Institute, the University of Tokyo, for their valuable comments. The authors also thank two anonymous reviewers and editor for their valuable comments on this manuscript.

References

Bluestein, H. B., 1993: *Synoptic-Dynamic Meteorology in Midlatitudes.* Vol. II, *Observations and Theory of Weather Systems.* Oxford University Press, 594pp.

Bosart, L. F., and F. H. Carr, 1978: A case study of excessive rainfall centered around Wellsville, New York, 20–21 June 1972. *Mon. Wea. Rev.*, **106**, 348–362.

Bosart, L. F., J. M. Cordeira, T. J. Galarneau Jr., B. J. Moore, and H. M. Archambault, 2012: An analysis of multiple predecessor rain events ahead of Tropical Cyclones Ike and Lowell: 10–15 September 2008. *Mon. Wea. Rev.*, **140**, 1081–1107.

Byun, K. Y., and T. Y. Lee, 2012: Remote effects of tropical cyclones on heavy rainfall over the Korean peninsula–statistical and composite analysis. *Tellus A*, **64**, 14983.

Cote, M. R., 2007: Predecessor rain events in advance of tropical cyclones. M.S. thesis, Dept. of Atmospheric and Environmental Sciences, University at Albany, State University of New York, 200 pp.

Galarneau, T. J. Jr., L. F. Bosart, and R. S. Schumacher, 2010: Predecessor rain events ahead of tropical cyclones. *Mon. Wea. Rev.*, **138**, 3272–3297.

Hersbach, H., B. Bell, P. Berrisford, G. Biavati, A. Horányi, J. Muñoz Sabater, J. Nicolas, C. Peubey, R. Radu, I. Rozum, D. Schepers, A. Simmons, C. Soci, D. Dee, J-N. Thépaut, 2018a: ERA5 hourly data on pressure levels from 1979 to present. Copernicus Climate Change Service (C3S) Climate Data Store (CDS). Accessed on 16 September 2020, 10.24381/cds.bd0915c6.

—— 2018b: ERA5 hourly data on single levels from 1979 to present. Copernicus Climate Change Service (C3S) Climate Data Store (CDS). Accessed on 17 July 2020, 10.24381/cds.adbb2d47.

—— 2019: ERA5 monthly averaged data on single levels from 1979 to present. Copernicus Climate Change Service (C3S) Climate Data Store (CDS). Accessed on 4 December 2020, 10.24381/cds.f17050d7.

Hirata, H., and R. Kawamura, 2014: Scale interaction between typhoons and the North Pacific subtropical high and associated remote effects during the Baiu/Meiyu season. *J. Geophys. Res.: Atmos.*, **119**, 5157–5170.

Hoskins, B. J., and M. A. Pedder, 1980: The diagnosis of middle latitude synoptic development. *Quart. J. Roy. Meteor. Soc.*, **106**, 707–719.

Kawamura, R., and T. Ogasawara, 2006: On the role of typhoons in generating PJ teleconnection patterns over the western North Pacific in late summer. *SOLA*, **2**, 37–40.

Kitabatake, N., 2002: The role of convective instability and frontogenetic circulation in the torrential rainfall in the Tokai District on 11-12 September 2000. *Pap. Meteor. Geophys.*, **53**, 91–108. (in Japanese)

Kitabatake, N., 2012: PRE (Predecessor Rain Event). *Tenki*, **59**, 171−172. (in Japanese)

Kitabatake, N., 2019: *Synoptic Meteorology (Basic edition).* Japan Meteorological Agency, 341pp. (in Japanese)

Kubota, T., S. Shige, H. Hashizume, K. Aonashi, N. Takahashi, S. Seto, M. Hirose, Y. N. Takayabu, K. Nakagawa, K. Iwanami, T. Ushio, M. Kachi, and K. Okamoto, 2007: Global Precipitation Map using Satellite-borne Microwave Radiometers by the GSMaP Project: Production and Validation. *IEEE Trans. Geosci. Remote Sens.*, **45**, 2259-2275.

Moore, B. J., L. F. Bosart, D. Keyser, and M. L. Jurewicz, 2013: Synoptic-scale environments of predecessor rain events occurring east of the Rocky Mountains in association with Atlantic basin tropical cyclones. *Mon. Wea. Rev.*, **141**, 1022–1047.

Murata, A., 2009: A mechanism for heavy precipitation over the Kii Peninsula accompanying Typhoon Meari (2004). *J. Meteor. Soc. Japan.*, **87**, 101–117.

Ninomiya, K., 2013: Influence of a distantly located typhoon, a weak westerly trough and orography on the intense rainfall on 14-15 September 1965 over Gifu and Fukui prefecture of Japan. *J. Meteor. Soc. Japan.*, **91**, 489–506.

Ogura, Y., 2000: *An Introduction to Synoptic-Dynamic Meteorology.* University of Tokyo Press, 289 pp. (in Japanese)

Ross, R. J., and Y. Kurihara, 1995: A numerical study on influences of Hurricane Gloria (1985) on the environment. *Mon. Wea. Rev.,* **123**, 332–346.

Saito, K., 2019: On the northward ageostrophic winds associated with a tropical cyclone. *SOLA*, **15**, 222–227.

Saito, K., and T. Matsunobu, 2020: Northward ageostrophic winds associated with a tropical cyclone. Part 2: Moisture transport and its impact on PRE. *SOLA*, **16**, 198–205.

Saito, K., T. Matsunobu, and T. Oizumi, 2022: Effect of upper-air moistening by northward ageostrophic winds associated with a tropical cyclone on the PRE enhancement. *SOLA*, **18**, 81–87.

Schumacher, R. S., and T. J. Galarneau Jr., 2012: Moisture transport into midlatitudes ahead of recurving tropical cyclones and its relevance in two predecessor rain events. *Mon. Wea. Rev.*, **140**, 1810–1827.

Schumacher, R. S., T. J. Galarneau Jr., and L. F. Bosart, 2011: Distant effects of a recurving tropical cyclone on rainfall in a midlatitude convective system: A high-impact predecessor rain event. *Mon. Wea. Rev.*, **139**, 650–667.

Sekizawa, S., T. Miyasaka, H. Nakamura, A. Shimpo, K. Takemura, and S. Maeda, 2019: Anomalous moisture transport and oceanic evaporation during a torrential rainfall event over western Japan in early July 2018. *SOLA*, **15A**, 25–30.

Tsuguti, H., and T. Kato, 2014: Objective extraction of heavy rainfall events and statistical analysis on their characteristic features. *Tenki*, **61**, 455–469. (in Japanese)

Wang, Y., Y. Wang, and H. Fudeyasu, 2009: The role of Typhoon Songda (2004) in producing distantly located heavy rainfall in Japan. *Mon. Wea. Rev.*, **137**, 3699–3716.

Yamada, K., and R. Kawamura, 2007: Dynamical link between typhoon activity and the PJ teleconnection pattern from early summer to autumn as revealed by the JRA-25 reanalysis. *SOLA*, **3**, 65–68.

Yoshida, K., and H. Itoh, 2012: Indirect effects of tropical cyclones on heavy rainfall events in Kyushu, Japan, during the Baiu season. *J. Meteor. Soc. Japan.*, **90**, 377–401.

Yoshikane, T., and F. Kimura, 2005: Climatic features of the water vapor transport around east Asia and rainfall over Japan in June and September, *Geophys. Res. Lett.*, **32**, L18712.

Yuan, J., D. Zhao, R. Yang, and H. Yang, 2018: Predecessor rain events over China's low-latitude highlands associated with Bay of Bengal tropical cyclones. *Climate Dyn.*, **50**, 825–843.

List of Figures

Fig. 1. (a) Locations of typhoon centers in the 58 PRE cases (blue dots). **(b)** Locations of precipitation centers in the 58 PRE cases (blue dots). **(c)** Same as in (a) but for the 31 non-PRE cases (blue dots). **(d)** Same as in (b) but for the 24 non-typhoon cases (blue dots). The red rectangle shows the extraction area [130–150°E, 30–40°N].

Fig. 2. (a–d) Tracks of typhoons in the PRE cases, divided into 10-year periods: 1980–1989, 1990–1999, 2000–2009, and 2010–2019. The blue dots show the typhoon centers. **(e–h)** Same as in (a–d) but for the non-PRE cases. The blue dots show the typhoon centers. The red rectangle shows the extraction area [130–150°E, 30–40°N].

Fig. 3. (a) Histogram of the distance (km) between typhoon centers and precipitation centers in the PRE cases. **(b)** Histogram of the direction of precipitation centers from typhoon centers in the PRE cases (azimuth; °), excluding four cases. **(c)** Histogram

of the central pressures (hPa) of typhoons in the PRE cases. **(d)** Same as in (c) but for the non-PRE cases.

Fig. 4. Histogram of typhoon central pressure (hPa) and maximum daily precipitation (mm) in the PRE cases, excluding one case.

Fig. 5. Composite of 500 hPa geopotential height (contour; m), precipitable water (shaded; mm) and vertical integrals of water vapor flux (vector; kg m^{-1} s^{-1}) for the 58 PRE cases on **(a)** Day–2, **(b)** Day–1, **(c)** Day0, and **(d)** Day+1. The contour interval is 60 m. The reference arrow is 400 kg m^{-1} s^{-1}. The red rectangle shows the extraction area [130–150°E, 30–40°N]. The green cross mark shows the median point of precipitation on Day0. The red dots on Day0 show the locations of typhoon centers relative to the median point of precipitation.

Fig. 6. Composite of 200 hPa geopotential height (black contour; dam), 200 hPa isotach (blue contour; m s^{-1}), 700 hPa vertical velocity (shaded; Pa s^{-1}) and 850 hPa horizontal wind (vector; m s^{-1}) for the 58 PRE cases on **(a)** Day–2, **(b)** Day–1, **(c)** Day0, and **(d)** Day+1. The black contour interval is 10 dam and the blue contour interval is 5 m s^{-1} (35–55 m s^{-1}). The reference arrow is 10 m s^{-1}. The red rectangle shows the extraction area [130–150°E, 30–40°N]. The green cross mark shows the median point of precipitation on Day0. The blue dots on Day0 show the locations of typhoon centers relative to the median point of precipitation.

Fig. 7. (a) Composite of 850 hPa equivalent potential temperature (shaded and contour; K)

for the 58 PRE cases on Day0. The contour interval is 3 K. The black rectangle shows the extraction area [130–150°E, 30–40°N]. The green cross mark shows the median point of precipitation. **(b)** Composite vertical cross-section of northward water vapor flux (shaded; g m^{-2} s^{-1}) for the 58 PRE cases on Day0 between 130°E and 150°E along the latitude 30°N.

Fig. 8. Composite of 500 hPa geopotential height (contour; m), precipitable water (shaded; mm) and vertical integrals of water vapor flux (vector; kg m^{-1} s^{-1}) for the 16 non-PRE cases on **(a)** Day–2, **(b)** Day–1, **(c)** Day0, and **(d)** Day+1. The contour interval is 60 m. The reference arrow is 400 kg m^{-1} s^{-1}. The red rectangle shows the extraction area [130–150°E, 30–40°N]. The red dots on Day0 show the locations of typhoon centers.

Fig. 9. Composite of 200 hPa geopotential height (black contour; dam), 200 hPa isotach (blue contour; m s^{-1}), 700 hPa vertical velocity (shaded; Pa s^{-1}) and 850 hPa horizontal wind (vector; m s^{-1}) for the 16 non-PRE cases on **(a)** Day–2, **(b)** Day–1, **(c)** Day0, and **(d)** Day+1. The black contour interval is 10 dam and the blue contour interval is 5 m s^{-1} (35–55 m s^{-1}). The reference arrow is 10 m s^{-1}. The red rectangle shows the extraction area [130–150°E, 30–40°N]. The blue dots on Day0 show the locations of typhoon centers.

Fig. 10. Composite of 850 hPa equivalent potential temperature (shaded and contour; K) for the 16 non-PRE cases on Day0. The contour interval is 3 K. The black rectangle

shows the extraction area [130–150°E, 30–40°N].

Fig. 11. Composite maps of the 24 non-typhoon cases on Day0. **(a)** 500 hPa geopotential height (contour; m), precipitable water (shaded; mm), and vertical integral of water vapor flux (vector; kg m^{-1} s^{-1}). The contour interval is 60 m. The reference arrow is 400 kg m^{-1} s^{-1}. The red rectangle shows the extraction area [130–150°E, 30–40°N]. The green cross mark shows the median point of precipitation. **(b)** 200 hPa geopotential height (black contour; dam), 200 hPa isotach (blue contour; m s^{-1}), 700 hPa vertical velocity (shaded; Pa s^{-1}) and 850 hPa horizontal wind (vector; m s^{-1}). The black contour interval is 10 dam and the blue contour interval is 5 m s^{-1} (35–55 m s^{-1}). The reference arrow is 10 m s^{-1}. **(c)** 850 hPa equivalent potential temperature (shaded and contour; K). The contour interval is 3 K. The black rectangle shows the extraction area [130–150°E, 30–40°N]. **(d)** Vertical cross-section of northward water vapor flux (shaded; g m^{-2} s^{-1}) between 130°E and 150°E along the latitude 30°N.

Fig. 12. Time series of composite for 500 hPa geopotential height (m) from Day–2 to Day0 (18 PRE cases, red; 16 non-PRE cases, blue). The 500 hPa geopotential height is averaged over the region [130–140°E, 27.5–32.5°N], and the value 48 hours before PRE occurrence is set to 0 m. The whisker marks represent standard deviation.

Fig. 13. Each component of the linear decomposition of composite vertical northward water vapor flux difference (not including air density ρ) on Day0 between 130°E and 150°E along the latitude 30°N (shaded; g kg^{-1} * m s^{-1}). **(a)** $\boldsymbol{q_{NT}} \cdot \Delta \boldsymbol{v}$, **(b)** $\Delta \boldsymbol{q} \cdot \boldsymbol{v_{NT}}$,

(c) $\Delta \boldsymbol{q} \cdot \Delta \boldsymbol{v}$.

Fig. 14. Composite of 700 hPa geopotential height (black contour; m), 700 hPa temperature (red contour; K), 800–600 hPa mean Q vector (vector; m^2 kg^{-1} s^{-1}) and 800–600 hPa mean divergence of Q vector (shaded; 10^{-18} m kg^{-1} s^{-1}, only $\nabla \cdot Q < 0$ is shown) on **(a)** Day0 PRE cases, **(b)** Day0 non-PRE cases, and **(c)** Day0 non-typhoon cases. The black contour interval is 30 m and the red contour interval is 3 K. The reference arrow is 2×10^{-13} m^2 kg^{-1} s^{-1}. The rectangle shows the extraction area [130–150°E, 30–40°N]. The green circle shows the median point of typhoons on Day0. The green triangle shows the median point of precipitation on Day0.

Fig. 15. Composite of 925 hPa geopotential height (black contour; m), 925 hPa temperature (red contour; K), and 925 hPa frontogenesis (shaded; 10^{-10} K m^{-1} s^{-1}) on **(a)** Day0 PRE cases, **(b)** Day0 non-PRE cases, and **(c)** Day0 non-typhoon cases. The black contour interval is 20 m and the red contour interval is 3 K. The rectangle shows the extraction area [130–150°E, 30–40°N]. The green circle shows the median point of typhoons on Day0. The green triangle shows the median point of precipitation on Day0. **(d)** Composite vertical cross-section of frontogenesis (solid black contour; 10^{-10} K m^{-1} s^{-1}), potential temperature (red contour; K), and vertical velocity (dashed black contour; Pa s^{-1}) on Day0 PRE cases. The solid black contour interval is 0.5×10^{-10} K m^{-1} s^{-1} (from 0.5 to 3.0 10^{-10} K m^{-1} s^{-1}), the red contour interval is 3 K and the dashed black contour is –0.1 Pa s^{-1} (from –0.55 to –0.05 Pa s^{-1}). The

location of the cross-sectional line is shown in (a).

Fig. 16. Conceptual models of the environmental field on **(a)** Day0 PRE cases and **(b)** Day0 non-PRE cases. The black contour shows the 200 hPa geopotential height. The dashed red contour shows the 850 hPa equivalent potential temperature (340 K). The orange arrow shows the horizontal wind. The rectangle shows the extraction area [130–150°E, 30–40°N]. The green circle shows the median point of typhoons. The green triangle shows the median point of precipitation.

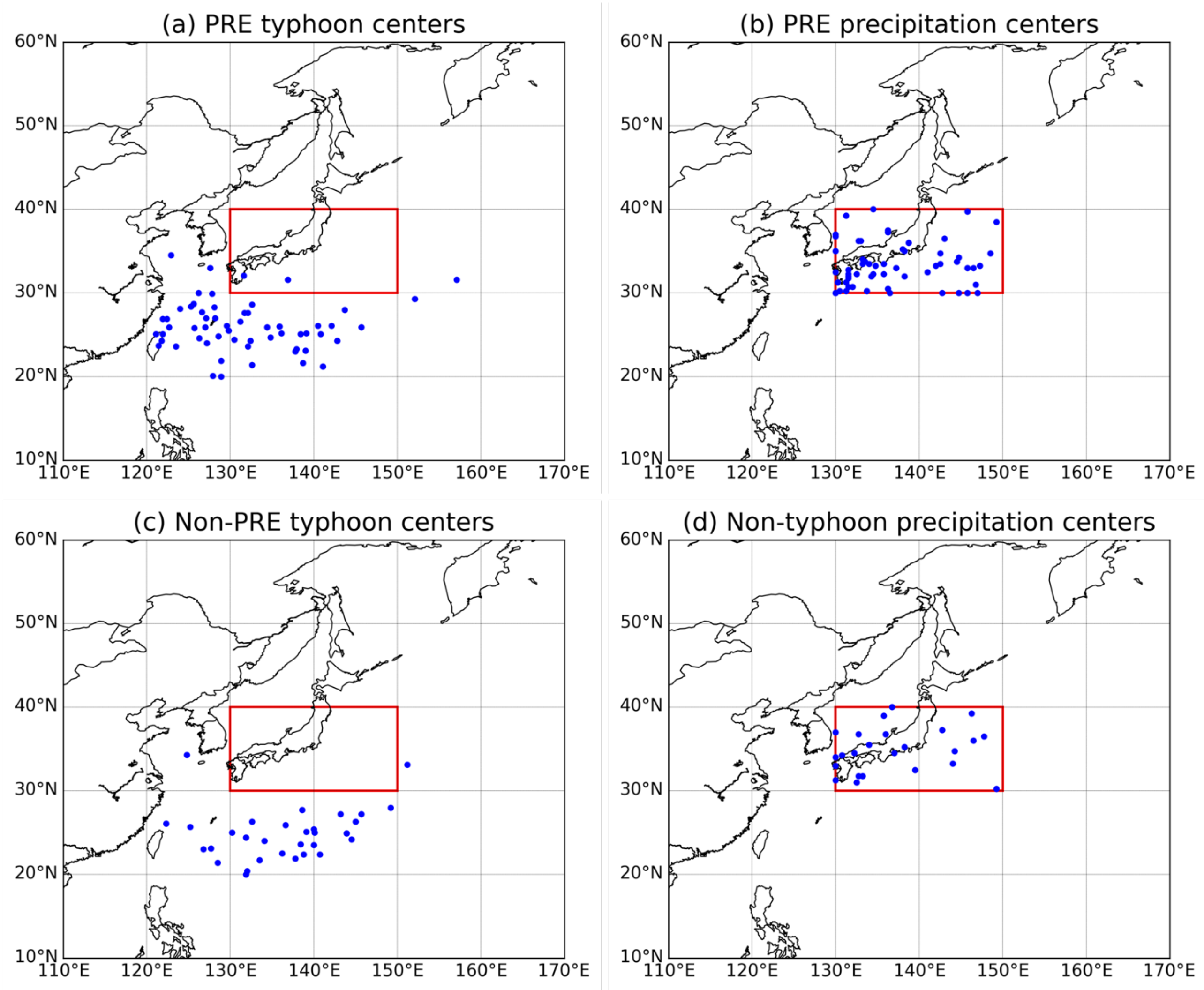

Fig. 1. (a) Locations of typhoon centers in the 58 PRE cases (blue dots). **(b)** Locations of precipitation centers in the 58 PRE cases (blue dots). **(c)** Same as in (a) but for the 31 non-PRE cases (blue dots). **(d)** Same as in (b) but for the 24 non-typhoon cases (blue dots). The red rectangle shows the extraction area [130–150°E, 30–40°N].

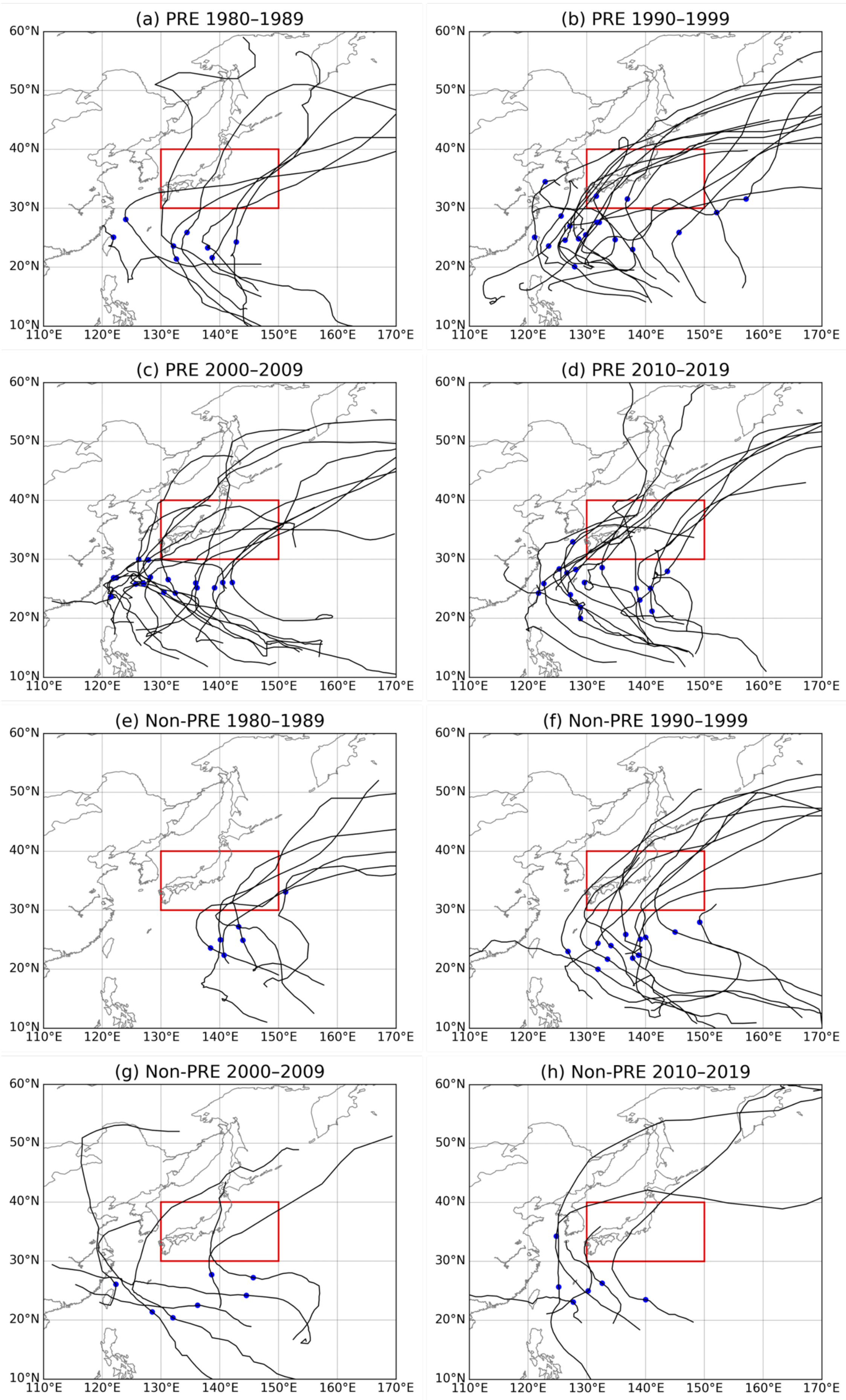
(a) PRE 1980–1989
(b) PRE 1990–1999
(c) PRE 2000–2009
(d) PRE 2010–2019
(e) Non-PRE 1980–1989
(f) Non-PRE 1990–1999
(g) Non-PRE 2000–2009
(h) Non-PRE 2010–2019
60°N
50°N
40°N
30°N
20°N
10°N
110°E
120°E
130°E
140°E
150°E
160°E
170°E

Fig. 2. (a–d) Tracks of typhoons in the PRE cases, divided into 10-year periods: 1980–1989, 1990–1999, 2000–2009, and 2010–2019. The blue dots show the typhoon centers. **(e–h)** Same as in (a–d) but for the non-PRE cases. The blue dots show the typhoon centers. The red rectangle shows the extraction area [130–150°E, 30–40°N].

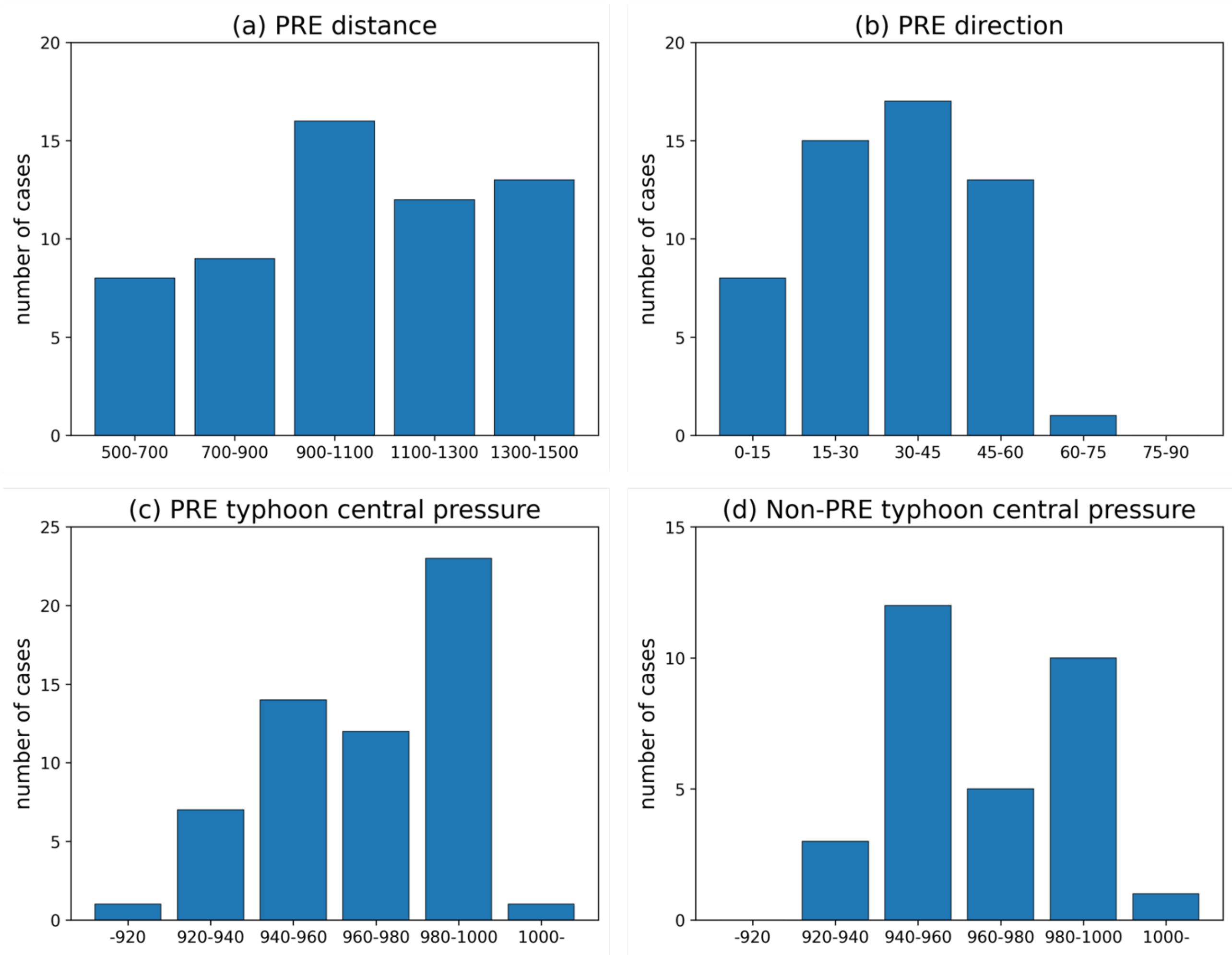

Fig. 3. (a) Histogram of the distance (km) between typhoon centers and precipitation centers in the PRE cases. **(b)** Histogram of the direction of precipitation centers from typhoon

centers in the PRE cases (azimuth; °), excluding four cases. **(c)** Histogram of the central pressures (hPa) of typhoons in the PRE cases. **(d)** Same as in (c) but for the non-PRE cases.

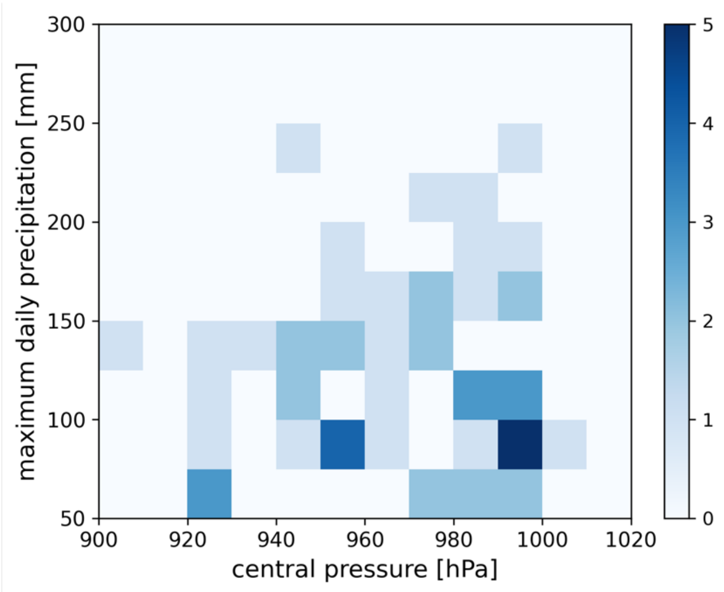

Fig. 4. Histogram of typhoon central pressure (hPa) and maximum daily precipitation (mm) in the PRE cases, excluding one case.

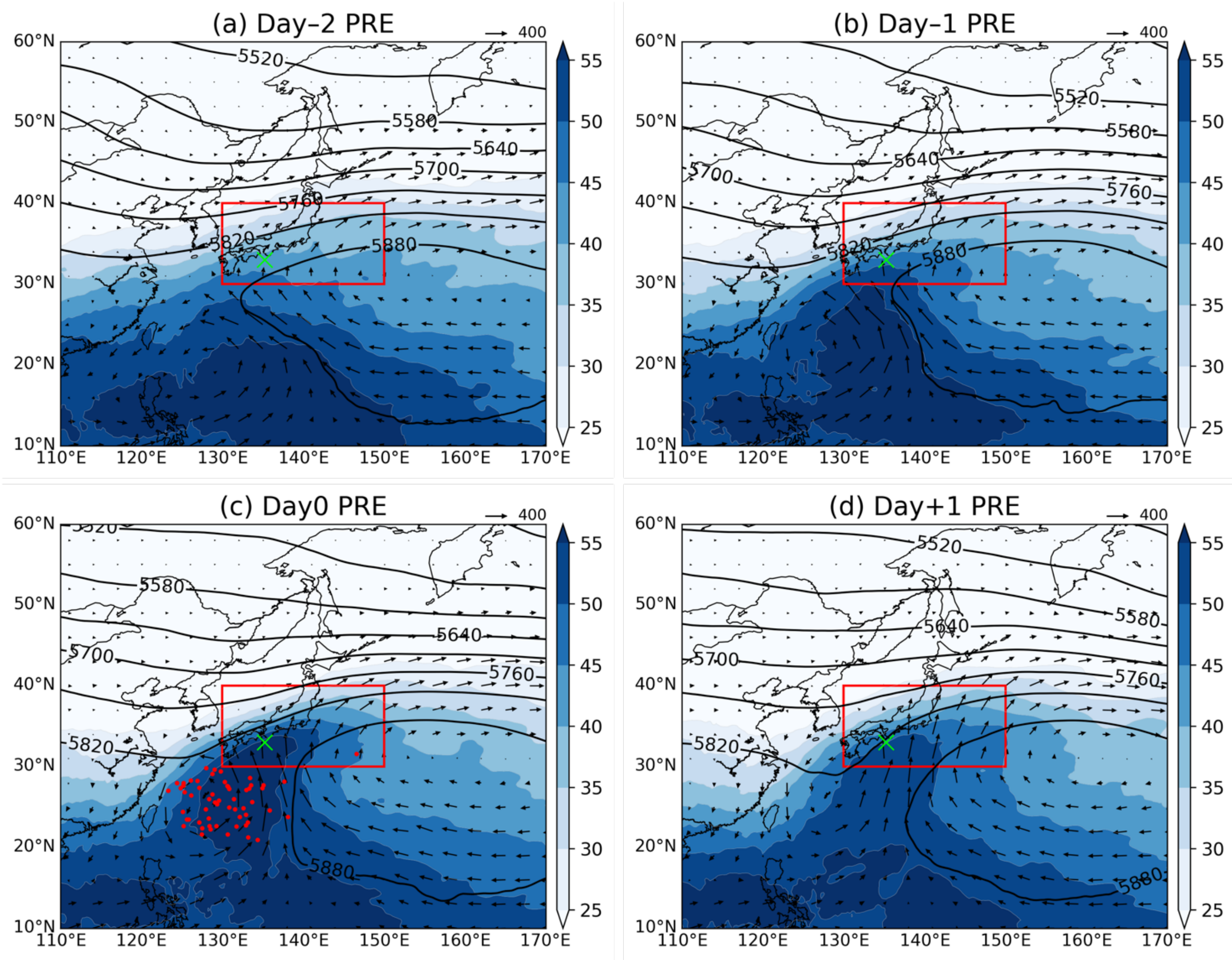

Fig. 5. Composite of 500 hPa geopotential height (contour; m), precipitable water (shaded; mm) and vertical integrals of water vapor flux (vector; kg m^{-1} s^{-1}) for the 58 PRE cases on **(a)** Day–2, **(b)** Day–1, **(c)** Day0, and **(d)** Day+1. The contour interval is 60 m. The reference arrow is 400 kg m^{-1} s^{-1}. The red rectangle shows the extraction area [130–150°E, 30–40°N]. The green cross mark shows the median point of precipitation on Day0. The red dots on Day0 show the locations of typhoon centers relative to the median point of precipitation.

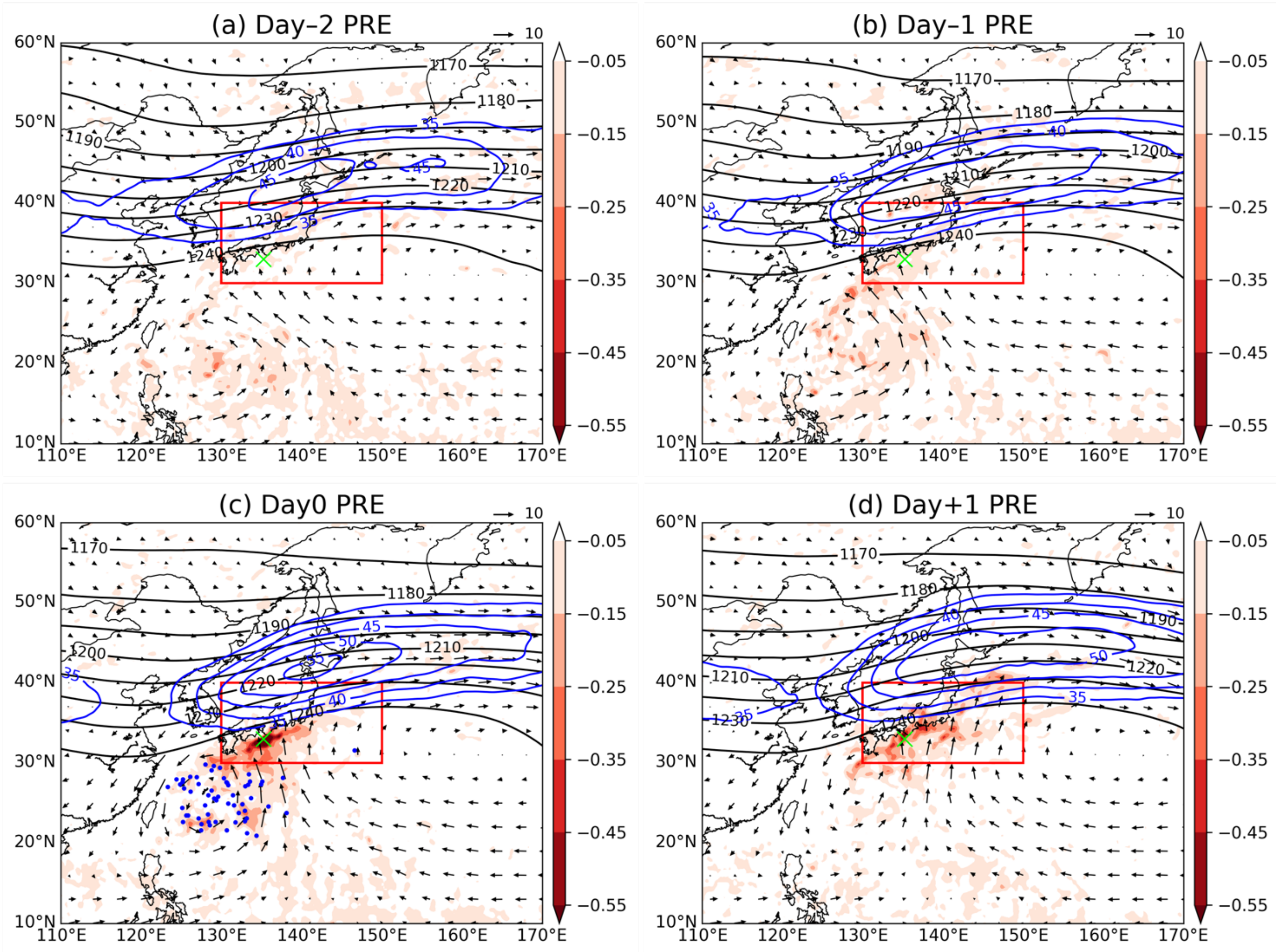

Fig. 6. Composite of 200 hPa geopotential height (black contour; dam), 200 hPa isotach (blue contour; m s^{-1}), 700 hPa vertical velocity (shaded; Pa s^{-1}) and 850 hPa horizontal wind (vector; m s^{-1}) for the 58 PRE cases on **(a)** Day–2, **(b)** Day–1, **(c)** Day0, and **(d)** Day+1. The black contour interval is 10 dam and the blue contour interval is 5 m s^{-1} (35–55 m s^{-1}). The reference arrow is 10 m s^{-1}. The red rectangle shows the extraction area [130–150°E, 30–40°N]. The green cross mark shows the median point of precipitation on Day0. The blue dots on Day0 show the locations of typhoon centers relative to the median point of precipitation.

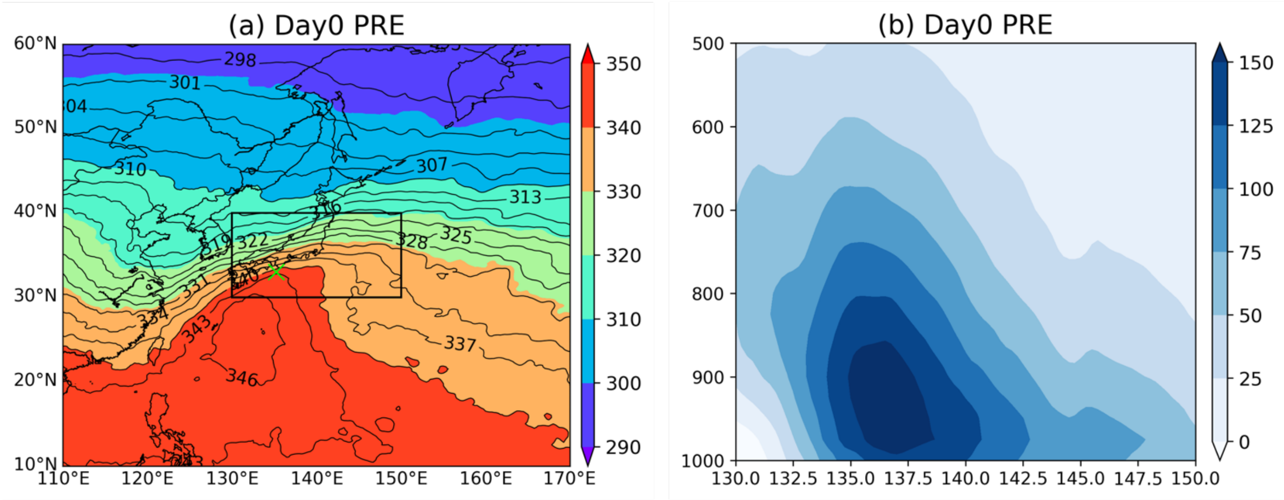

Fig. 7. (a) Composite of 850 hPa equivalent potential temperature (shaded and contour; K) for the 58 PRE cases on Day0. The contour interval is 3 K. The black rectangle shows the extraction area [130–150°E, 30–40°N]. The green cross mark shows the median point of precipitation. **(b)** Composite vertical cross-section of northward water vapor flux (shaded; g m^{-2} s^{-1}) for the 58 PRE cases on Day0 between 130°E and 150°E along the latitude 30°N.

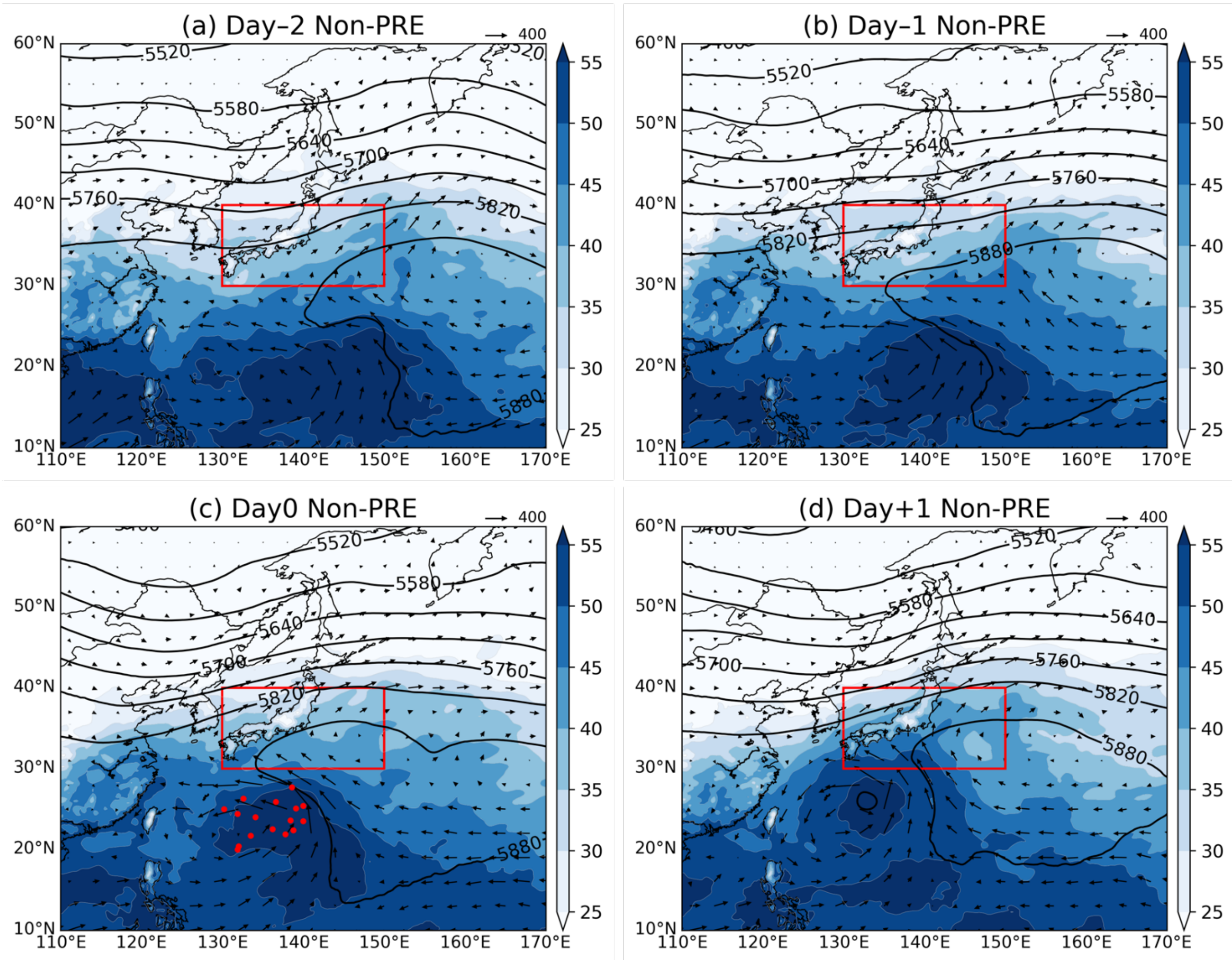

Fig. 8. Composite of 500 hPa geopotential height (contour; m), precipitable water (shaded; mm) and vertical integrals of water vapor flux (vector; kg m^{-1} s^{-1}) for the 16 non-PRE cases on **(a)** Day–2, **(b)** Day–1, **(c)** Day0, and **(d)** Day+1. The contour interval is 60 m. The reference arrow is 400 kg m^{-1} s^{-1}. The red rectangle shows the extraction area [130–150°E, 30–40°N]. The red dots on Day0 show the locations of typhoon centers.

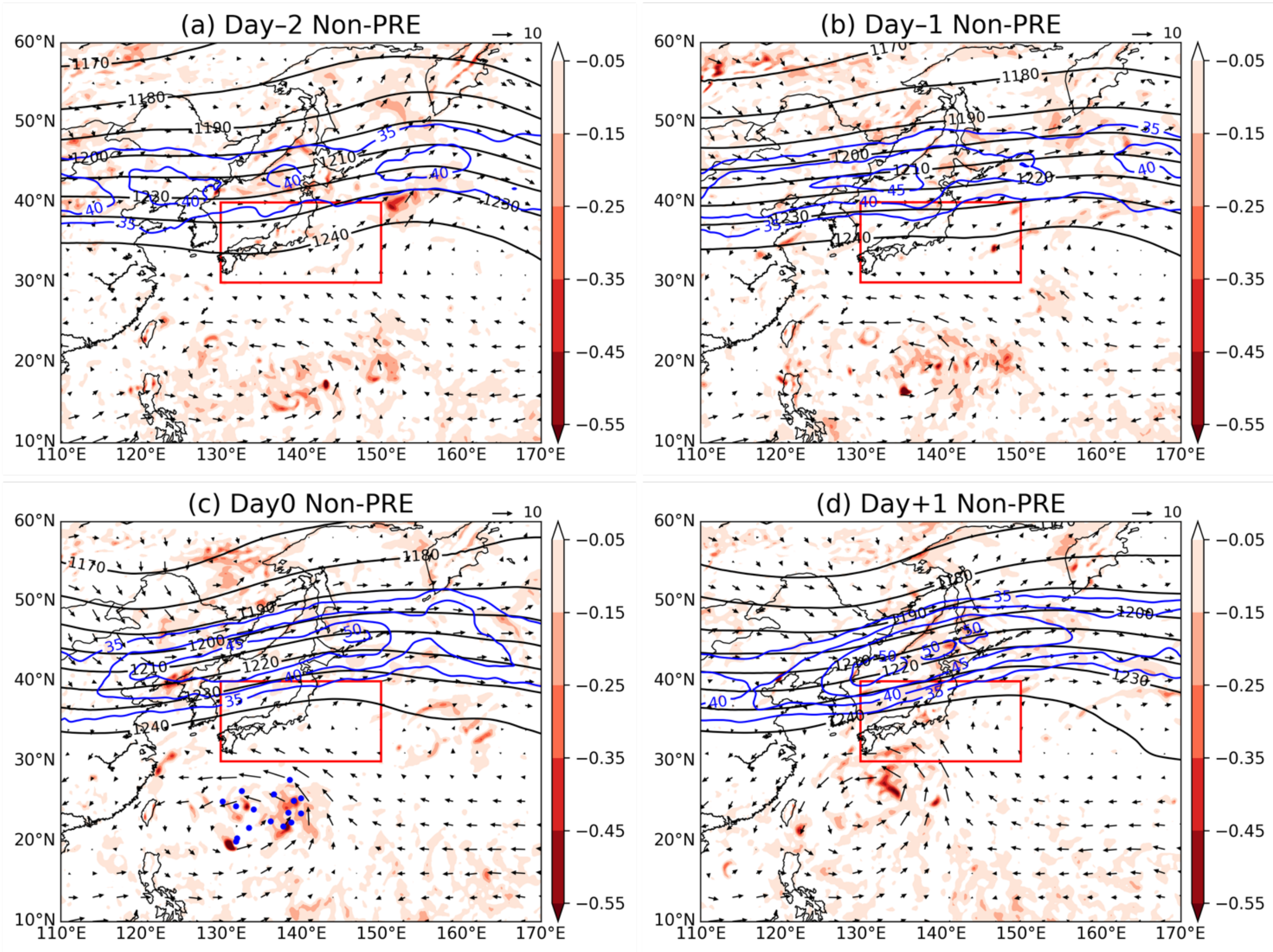

Fig. 9. Composite of 200 hPa geopotential height (black contour; dam), 200 hPa isotach (blue contour; m s^{-1}), 700 hPa vertical velocity (shaded; Pa s^{-1}) and 850 hPa horizontal wind (vector; m s^{-1}) for the 16 non-PRE cases on **(a)** Day–2, **(b)** Day–1, **(c)** Day0, and **(d)** Day+1. The black contour interval is 10 dam and the blue contour interval is 5 m s^{-1} (35–55 m s^{-1}). The reference arrow is 10 m s^{-1}. The red rectangle shows the extraction area [130–150°E, 30–40°N]. The blue dots on Day0 show the locations of typhoon centers.

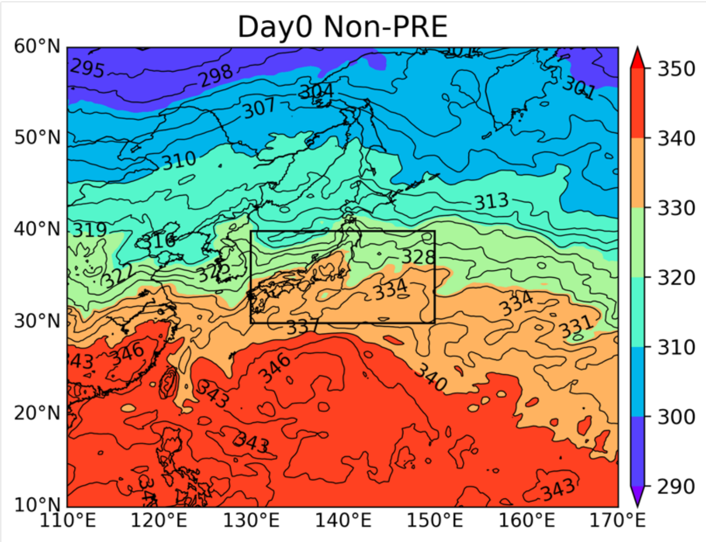

Fig. 10. Composite of 850 hPa equivalent potential temperature (shaded and contour; K) for the 16 non-PRE cases on Day0. The contour interval is 3 K. The black rectangle shows the extraction area [130–150°E, 30–40°N].

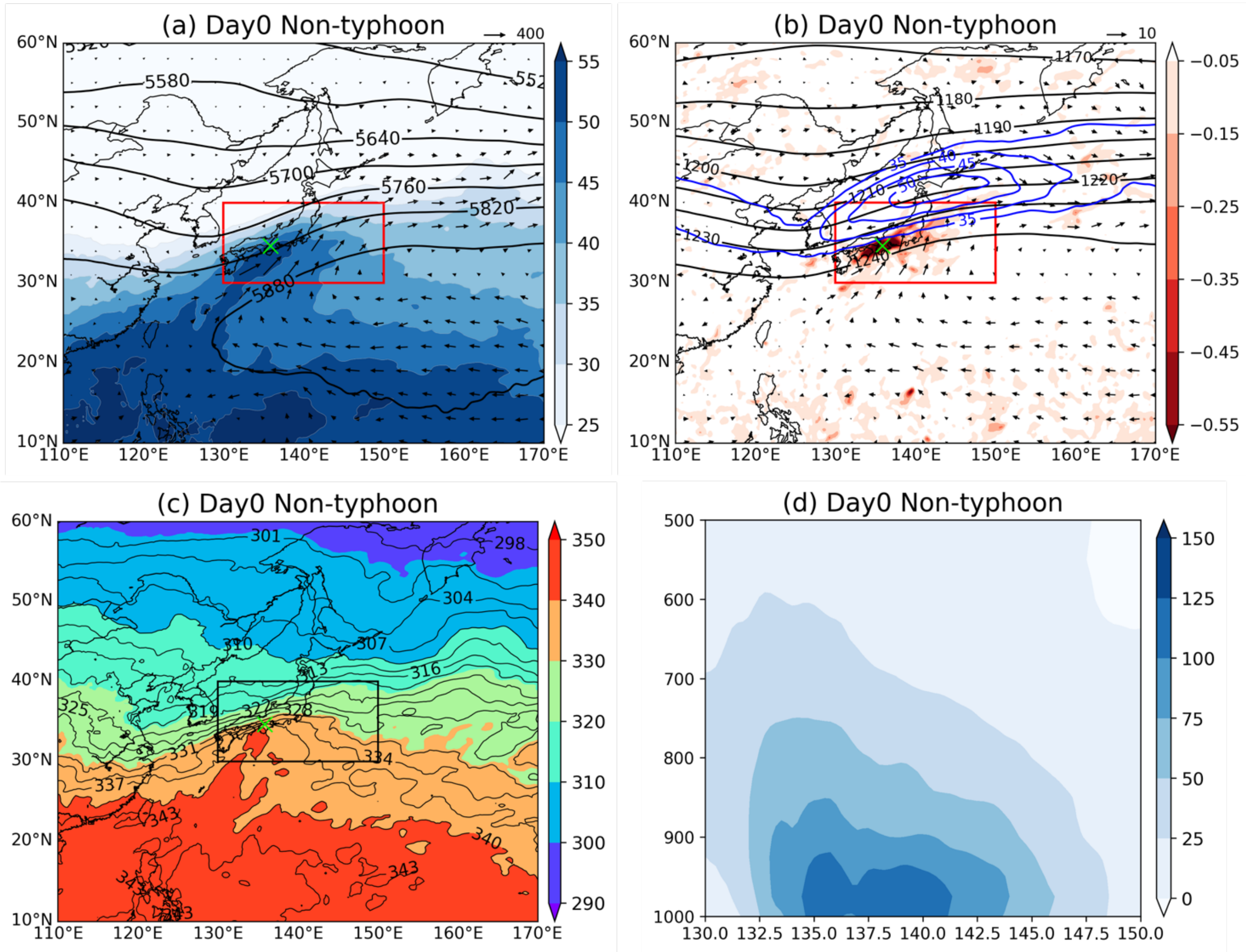

Fig. 11. Composite maps of the 24 non-typhoon cases on Day0. **(a)** 500 hPa geopotential height (contour; m), precipitable water (shaded; mm), and vertical integral of water vapor flux (vector; kg m^{-1} s^{-1}). The contour interval is 60 m. The reference arrow is 400 kg m^{-1} s^{-1}. The red rectangle shows the extraction area [130–150°E, 30–40°N]. The green cross mark shows the median point of precipitation. **(b)** 200 hPa geopotential height (black contour; dam), 200 hPa isotach (blue contour; m s^{-1}), 700 hPa vertical velocity (shaded; Pa s^{-1}) and 850 hPa horizontal wind (vector; m s^{-1}). The black contour interval is 10 dam and the blue contour interval is 5 m s^{-1} (35–55 m s^{-1}). The reference arrow is 10 m s^{-1}.

(c) 850 hPa equivalent potential temperature (shaded and contour; K). The contour interval is 3 K. The black rectangle shows the extraction area [130–150°E, 30–40°N]. **(d)** Vertical cross-section of northward water vapor flux (shaded; g m^{-2} s^{-1}) between 130°E and 150°E along the latitude 30°N.

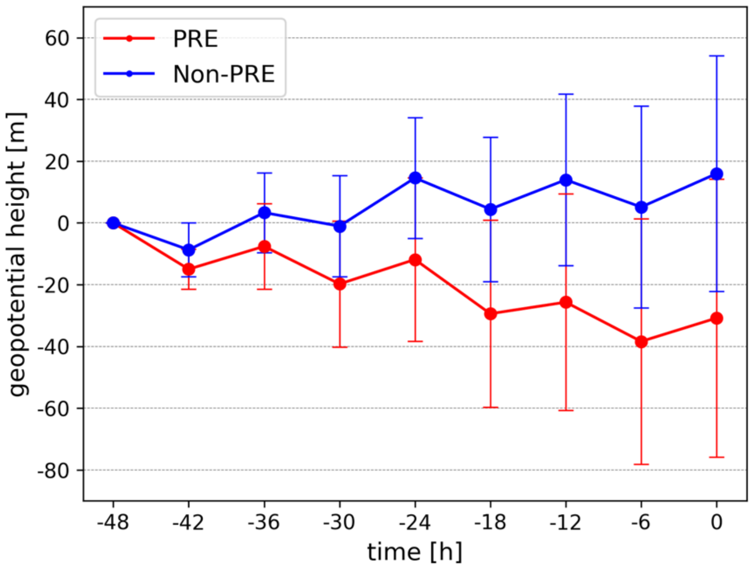

Fig. 12. Time series of composite for 500 hPa geopotential height (m) from Day–2 to Day0 (18 PRE cases, red; 16 non-PRE cases, blue). The 500 hPa geopotential height is averaged over the region [130–140°E, 27.5–32.5°N], and the value 48 hours before PRE occurrence is set to 0 m. The whisker marks represent standard deviation.

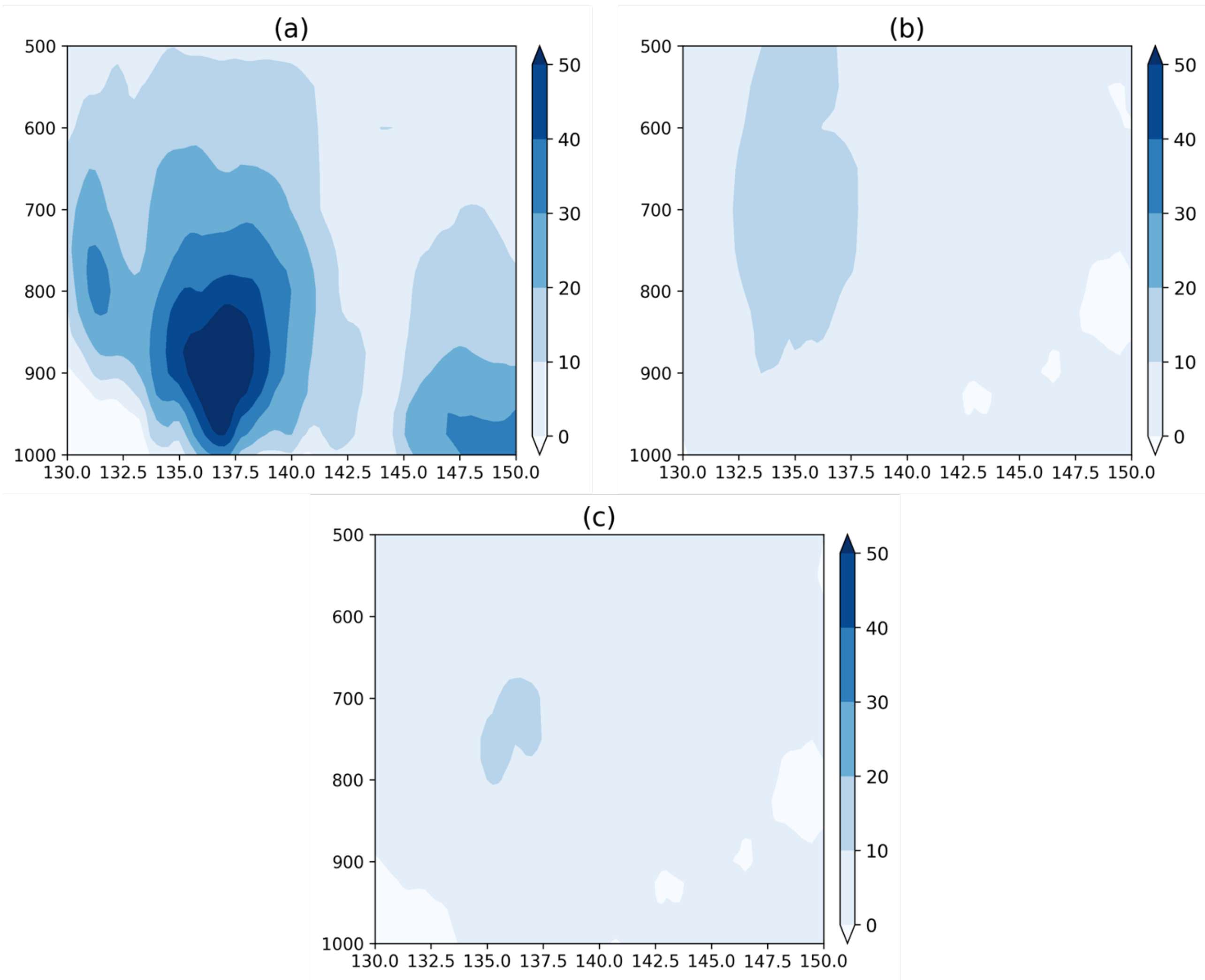

Fig. 13. Each component of the linear decomposition of composite vertical northward water vapor flux difference (not including air density ρ) on Day0 between 130°E and 150°E along the latitude 30°N (shaded; g kg^{-1} * m s^{-1}). **(a)** $\boldsymbol{q_{NT}} \cdot \Delta \boldsymbol{v}$, **(b)** $\Delta \boldsymbol{q} \cdot \boldsymbol{v_{NT}}$, **(c)** $\Delta \boldsymbol{q} \cdot \Delta \boldsymbol{v}$.

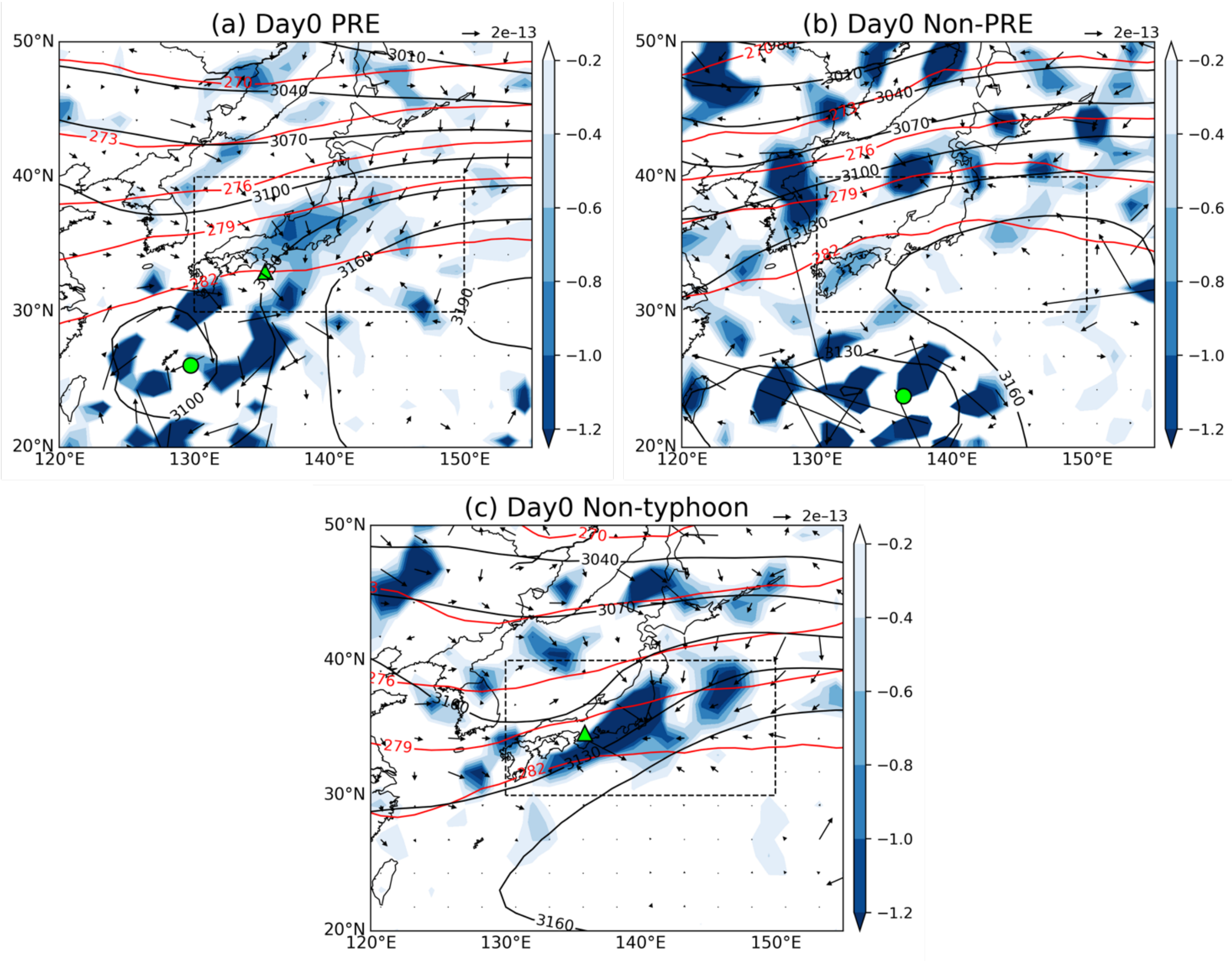

Fig. 14. Composite of 700 hPa geopotential height (black contour; m), 700 hPa temperature (red contour; K), 800–600 hPa mean Q vector (vector; m^2 kg^{-1} s^{-1}) and 800–600 hPa mean divergence of Q vector (shaded; 10^{-18} m kg^{-1} s^{-1}, only $\nabla \cdot Q < 0$ is shown) on **(a)** Day0 PRE cases, **(b)** Day0 non-PRE cases, and **(c)** Day0 non-typhoon cases. The black contour interval is 30 m and the red contour interval is 3 K. The reference arrow is 2×10^{-13} m^2 kg^{-1} s^{-1}. The rectangle shows the extraction area [130–150°E, 30–40°N]. The green circle shows the median point of typhoons on Day0. The green triangle shows the median point of precipitation on Day0.

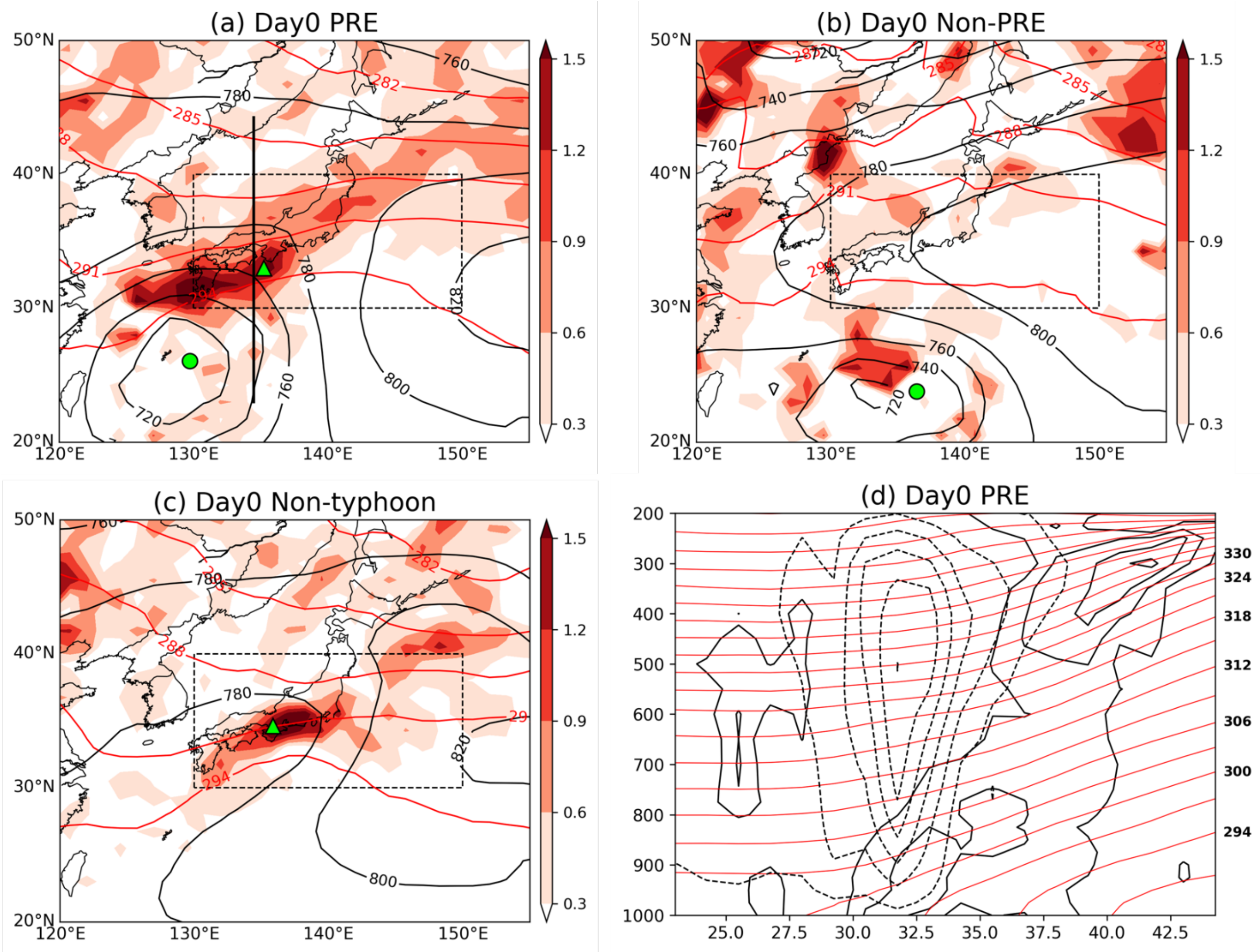

Fig. 15. Composite of 925 hPa geopotential height (black contour; m), 925 hPa temperature (red contour; K), and 925 hPa frontogenesis (shaded; 10^{-10} K m^{-1} s^{-1}) on **(a)** Day0 PRE cases, **(b)** Day0 non-PRE cases, and **(c)** Day0 non-typhoon cases. The black contour interval is 20 m and the red contour interval is 3 K. The rectangle shows the extraction area [130–150°E, 30–40°N]. The green circle shows the median point of typhoons on Day0. The green triangle shows the median point of precipitation on Day0. **(d)** Composite vertical cross-section of frontogenesis (solid black contour; 10^{-10} K m^{-1} s^{-1}), potential temperature (red contour; K), and vertical velocity (dashed black contour; Pa s^{-1}) on

Day0 PRE cases. The solid black contour interval is 0.5×10^{-10} K m^{-1} s^{-1} (from 0.5 to 3.0 10^{-10} K m^{-1} s^{-1}), the red contour interval is 3 K and the dashed black contour is –0.1 Pa s^{-1} (from –0.55 to –0.05 Pa s^{-1}). The location of the cross-sectional line is shown in (a).

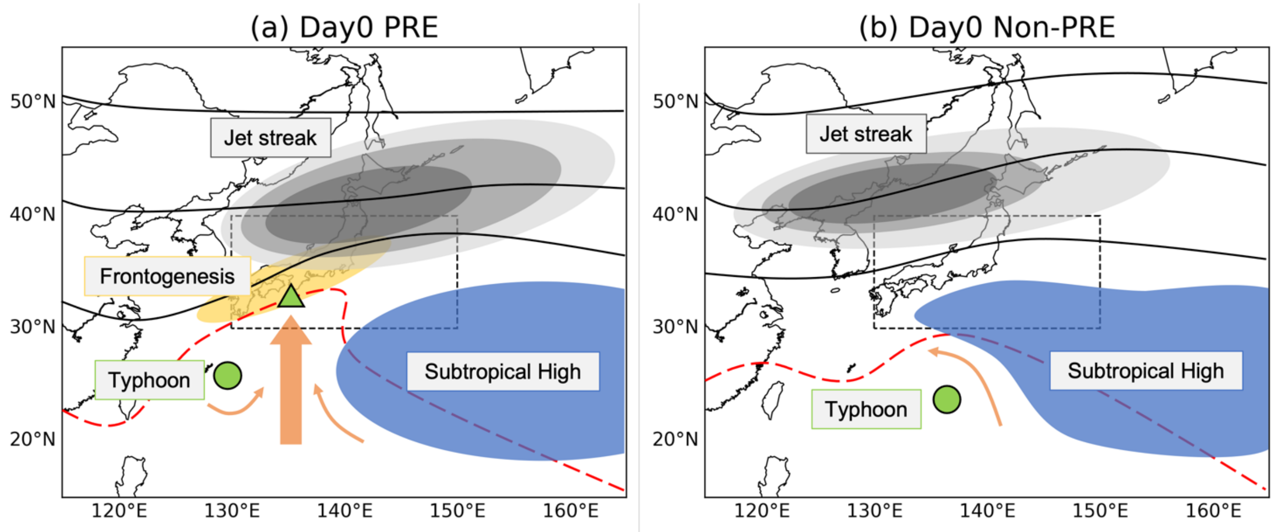

Fig. 16. Conceptual models of the environmental field on **(a)** Day0 PRE cases and **(b)** Day0 non-PRE cases. The black contour shows the 200 hPa geopotential height. The dashed red contour shows the 850 hPa equivalent potential temperature (340 K). The orange arrow shows the horizontal wind. The rectangle shows the extraction area [130–150°E, 30–40°N]. The green circle shows the median point of typhoons. The green triangle shows the median point of precipitation.

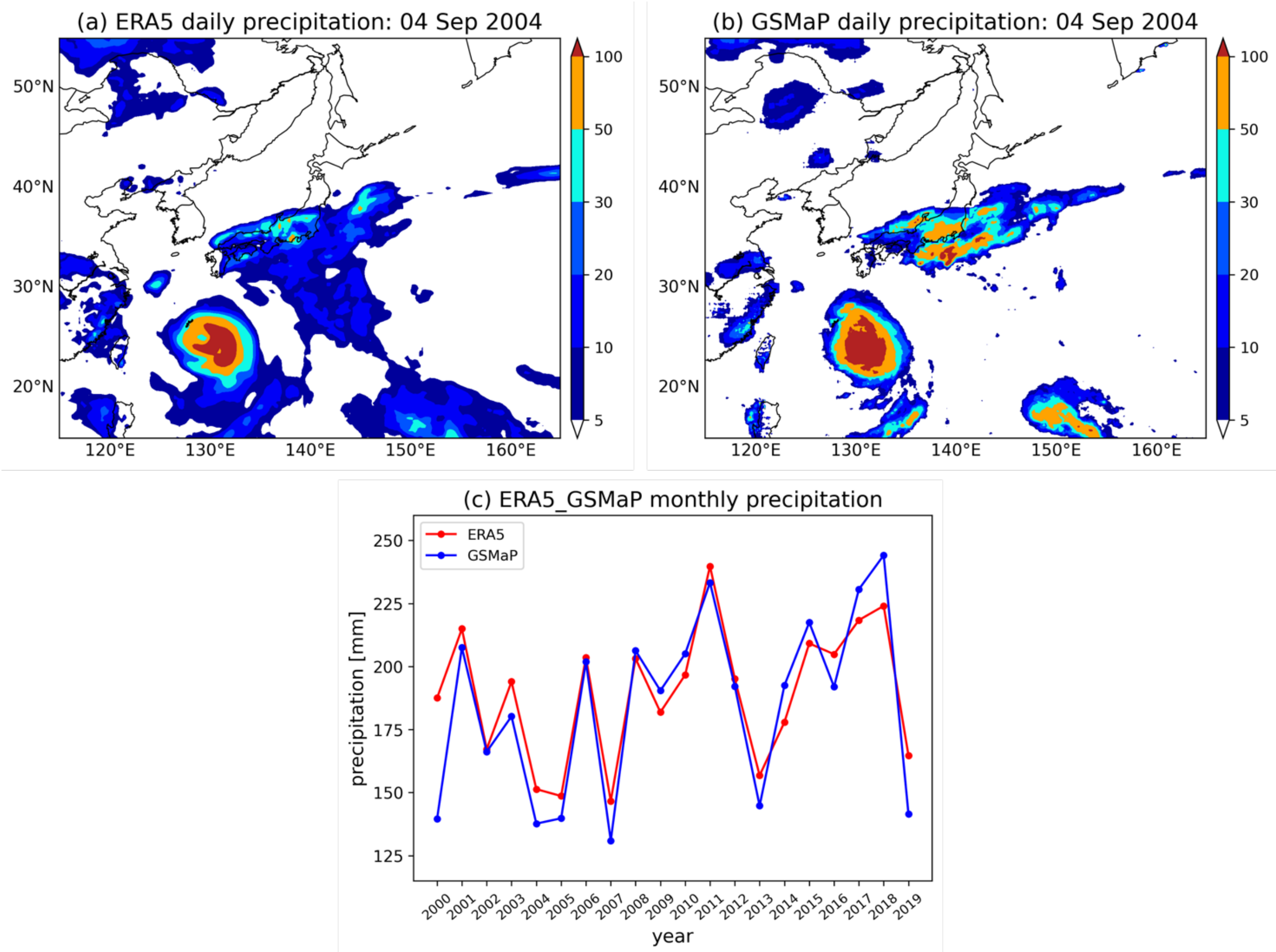

Supplement 1. (a) Daily precipitation (shaded; mm) on 04 September 2004 using the ERA5 data. **(b)** Same as in (a) but for using the GSMaP data. **(c)** Time series of monthly precipitation in September (mm) from 2000 to 2019 (ERA5, red; GSMaP blue). The monthly precipitation is averaged over the region [130–150°E, 30–40°N].

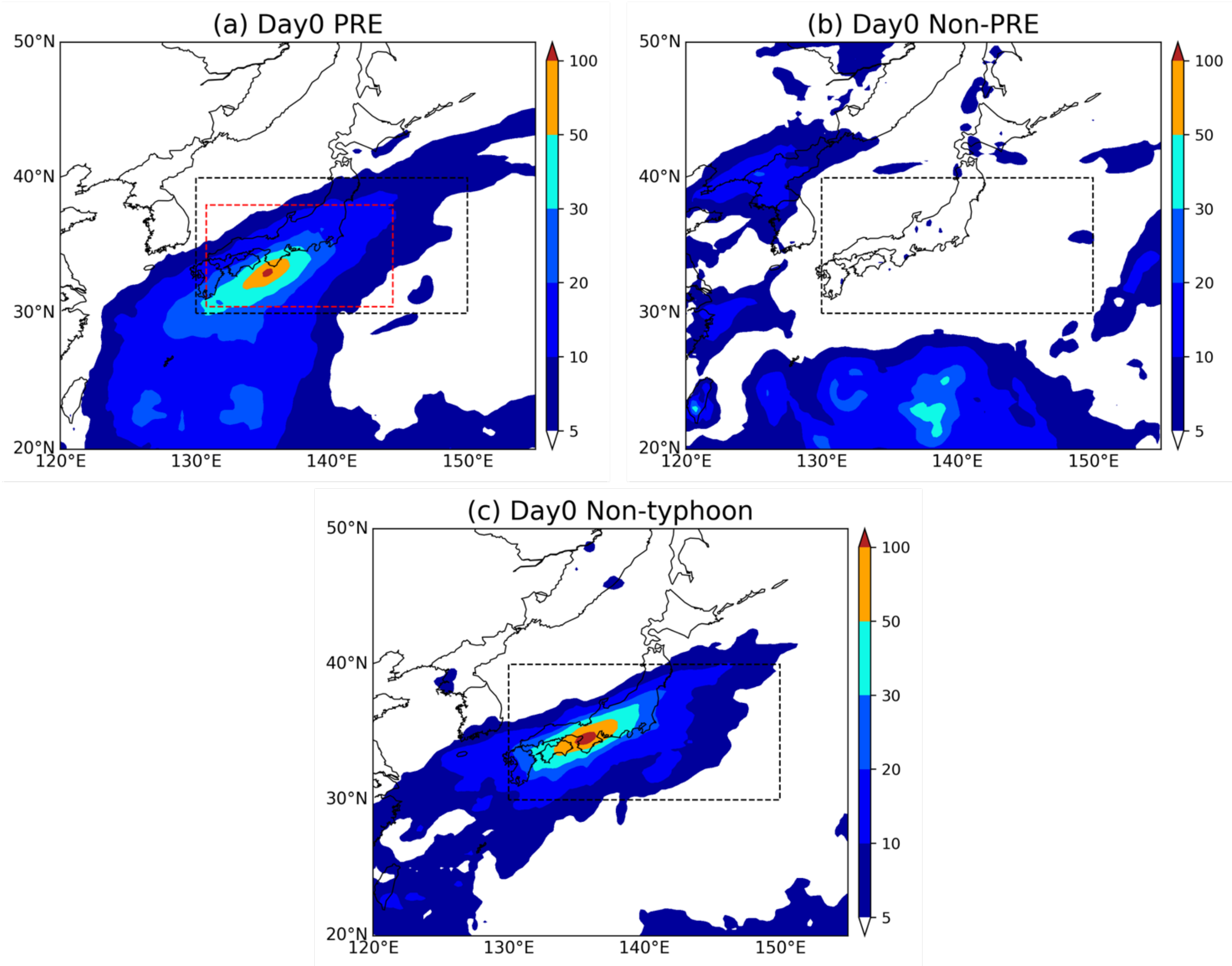

Supplement 2. Composite of daily precipitation (shaded; mm) on **(a)** Day0 PRE cases, **(b)** Day0 non-PRE cases, and **(c)** Day0 non-typhoon cases. The black rectangle shows the extraction area [130–150°E, 30–40°N]. The red rectangle shows the Welch's t-test area [130.75–144.5°E, 30.5–38°N].